Article

Developmental Cell

Vangl-dependent mesenchymal thinning shapes the distal lung during murine sacculation

Graphical abstract

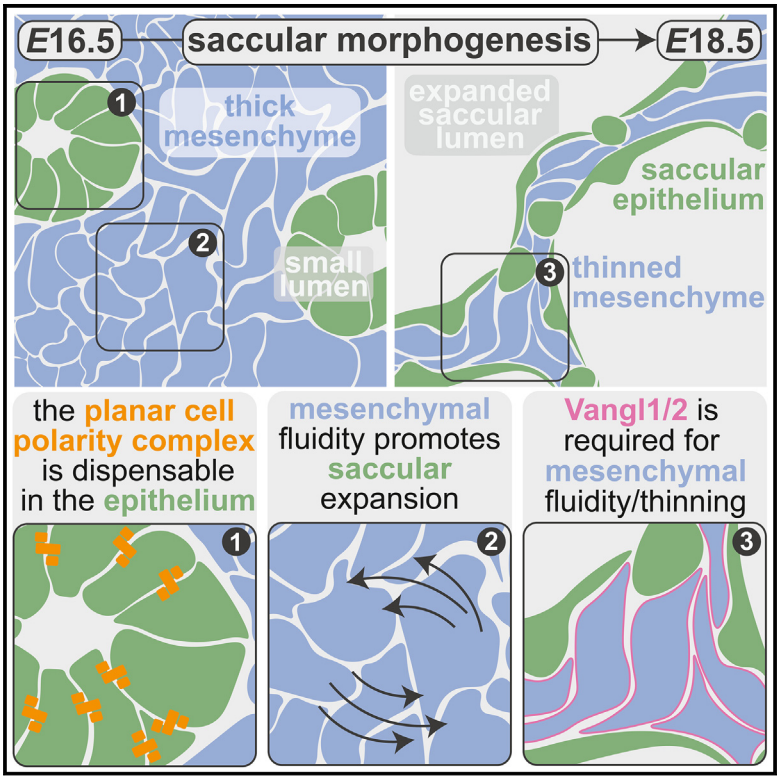

Highlights

- Core planar cell polarity complex function is dispensable for lung morphogenesis
- *Vangl1/2* is required in the lung mesenchyme for sacculation
- *In silico* modeling indicates that a fluid mesenchyme supports sacculation
- *Vangl* mutants exhibit altered cell shapes, consistent with reduced tissue fluidity

Authors

Sarah V. Paramore, Carolina Trenado-Yuste, Rishabh Sharan, Celeste M. Nelson, Danelle Devenport

Correspondence

celesten@princeton.edu (C.M.N.), danelle@princeton.edu (D.D.)

In brief

Paramore et al. demonstrate that the planar cell polarity (PCP) complex is dispensable for murine lung morphogenesis. Rather, the PCP component Vangl is specifically required in the mesenchyme for lung sacculation. *Vangl*-mutant mesenchymal cells exhibit altered cell morphologies, disrupting the mesenchymal fluidity that promotes sacculation.

Paramore et al., 2024, Developmental Cell *59*, 1–15
May 20, 2024
https://doi.org/10.1016/j.devcel.2024.03.010

CellPress

Please cite this article in press as: Paramore et al., *Vangl*-dependent mesenchymal thinning shapes the distal lung during murine sacculation, Developmental Cell (2024), https://doi.org/10.1016/j.devcel.2024.03.010

Developmental Cell

CellPress

Article

Vangl-dependent mesenchymal thinning shapes the distal lung during murine sacculation

Sarah V. Paramore,[1] Carolina Trenado-Yuste,[2,3] Rishabh Sharan,[3] Celeste M. Nelson,[1,2,*] and Danelle Devenport[1,4,*]
[1]Department of Molecular Biology, Princeton University, Princeton, NJ 08544, USA
[2]Department of Chemical & Biological Engineering, Princeton University, Princeton, NJ 08544, USA
[3]Lewis-Sigler Institute for Integrative Genomics, Princeton University, Princeton, NJ 08544, USA
[4]Lead contact
*Correspondence: celesten@princeton.edu (C.M.N.), danelle@princeton.edu (D.D.)
https://doi.org/10.1016/j.devcel.2024.03.010

SUMMARY

The planar cell polarity (PCP) complex is speculated to function in murine lung development, where branching morphogenesis generates an epithelial tree whose distal tips expand dramatically during sacculation. Here, we show that PCP is dispensable in the airway epithelium for sacculation. Rather, we find a *Celsr1*-independent role for the PCP component *Vangl* in the pulmonary mesenchyme: loss of *Vangl1/2* inhibits mesenchymal thinning and expansion of the saccular epithelium. Further, loss of mesenchymal *Wnt5a* mimics sacculation defects observed in *Vangl2*-mutant lungs, implicating mesenchymal Wnt5a/Vangl signaling as a key regulator of late lung morphogenesis. A computational model predicts that sacculation requires a fluid mesenchymal compartment. Lineage-tracing and cell-shape analyses are consistent with the mesenchyme acting as a fluid tissue, suggesting that loss of *Vangl1/2* impacts the ability of mesenchymal cells to exchange neighbors. Our data thus identify an explicit function for *Vangl* and the pulmonary mesenchyme in actively shaping the saccular epithelium.

INTRODUCTION

During development of the mammalian lung, the pulmonary epithelium undergoes dozens of rounds of stereotyped branching to form a complex airway tree.[1] After branching is completed, the lungs undergo the canalicular and saccular stages of development. The pulmonary mesenchyme thins, while distal airways widen dramatically to increase epithelial surface area, forming saccules. Concurrently, the saccular epithelium differentiates into specialized cell types, including type I and type II alveolar cells, preparing the lung to function after birth.[2,3] Understanding the processes that drive sacculation is essential for motivating new strategies to treat defects associated with prematurity and congenital abnormalities.

During sacculation, the mesenchyme between distal airways thins to a roughly single-cell layer as the epithelium expands. This rapid change in tissue shape results in an increase in epithelial surface area that supports gas exchange postnatally. Although the specific cellular mechanisms that underlie epithelial expansion and mesenchymal thinning are unknown, decades of studies have made clear that mechanical forces generated by lumenal fluid pressure are an important driver of sacculation. For example, fetal breathing movements, which begin at approximately *E*16 in mice, lead to cyclic increases in fluid pressure and promote sacculation.[4–6] Conversely, sacculation is halted when the pressure in the lung is reduced by leakage of amniotic fluid[7] or by ablation of fetal breathing movements via loss of skeletal muscle,[8] leading to lung hypoplasia. Pressure of the fluid within the lung has a direct effect on the fate of alveolar epithelial cells (AECs): those exposed to high pressure differentiate into type I AECs (AEC1s), whereas those exposed to low pressure differentiate into type II AECs (AEC2s).[9] However, it is unknown whether pressure also regulates mesenchymal thinning. One could posit that a high lumenal fluid pressure may push mesenchymal cells into a thin layer, as increasing the pressure of this fluid increases the overall rate of lung development.[10,11] Mesenchymal cells might also play an active role in rearranging both themselves and the surrounding extracellular matrix (ECM) to facilitate saccular expansion.

The core planar cell polarity (PCP) complex was recently implicated in the process of sacculation.[12,13] The core PCP complex consists of three transmembrane proteins (in mice, Celsr1–3, Vangl1/2, and Fzd3/6[14]) that localize asymmetrically along the plane of a tissue and regulate oriented cell behaviors.[15] To generate asymmetry and relay polarity information, Vangl/Celsr localize to the opposite side of the cell as Fzd/Celsr. The Celsr cadherin repeats mediate the formation of PCP junctions between neighboring cells (Figure 1A). This asymmetric localization is indicative of and required for PCP function. In vertebrates, PCP regulates cytoskeletal organization and is required for convergent-extension movements during gastrulation and neural tube closure.[14,16–20] Similarly, PCP regulates the shape of epithelial tubules in the developing kidney via convergent extension.[21,22] In the lung, the role of PCP is beginning to be

Please cite this article in press as: Paramore et al., *Vangl*-dependent mesenchymal thinning shapes the distal lung during murine sacculation, Developmental Cell (2024), https://doi.org/10.1016/j.devcel.2024.03.010

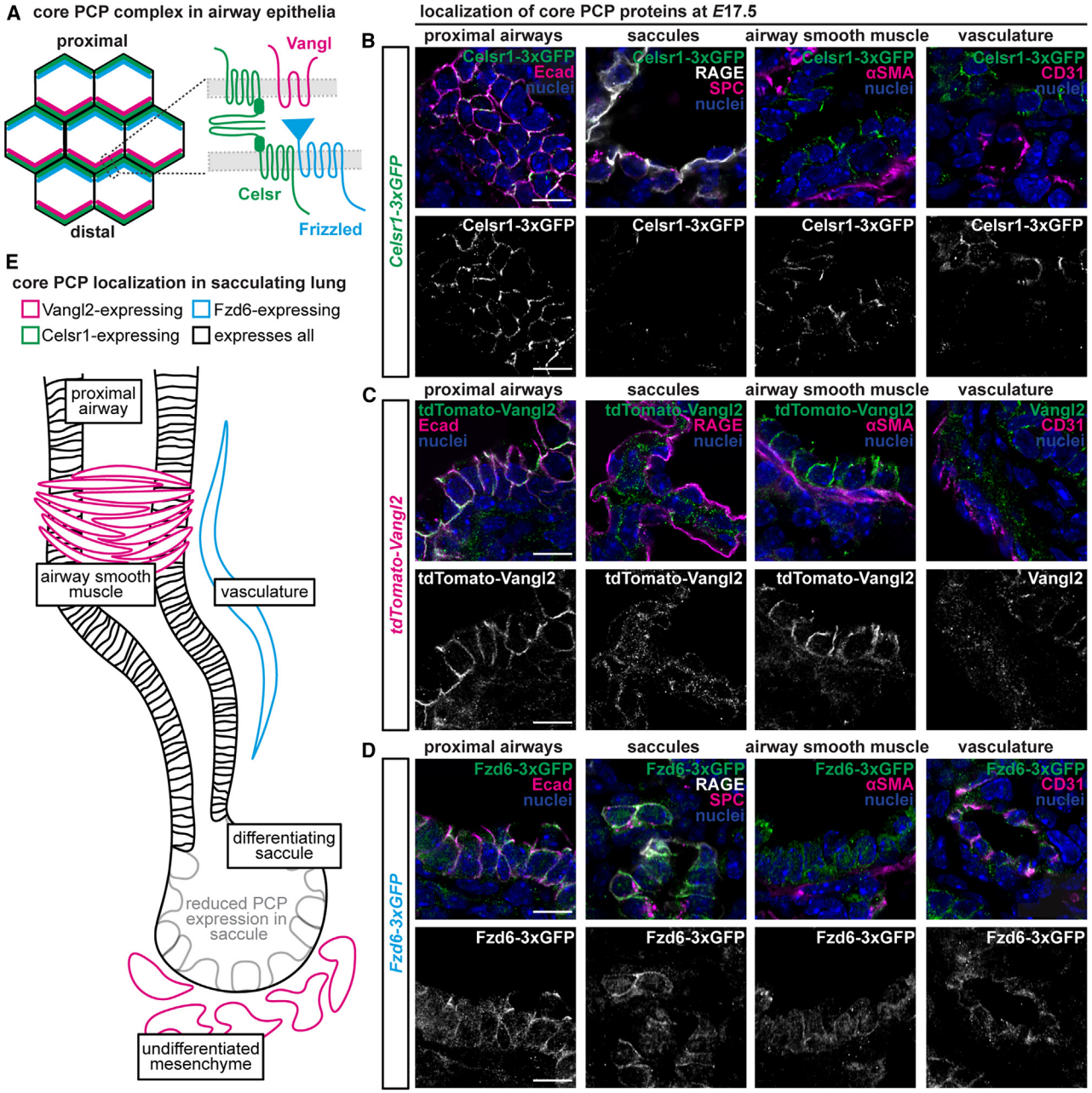

Figure 1. Core PCP proteins are differentially expressed in sacculation-stage lungs

(A) Schematic illustrating the PCP complex in a planar epithelial tissue.

(B) Representative images of 10-μm-thick sections of *E*17.5 lungs showing localization of Celsr1-3xGFP in proximal airways (Ecad), saccules (receptor for advanced glycation end products (RAGE) and surfactant protein C (SPC)), airway smooth muscle (αSMA), and vasculature (CD31).

(C) Representative images of 10-μm-thick sections of *E*17.5 lungs showing localization of tdTomato-Vangl2 or Vangl2 in proximal airways (Ecad), saccules (RAGE and SPC), airway smooth muscle (αSMA), and vasculature (CD31).

(D) Representative images of 10-μm-thick sections of *E*17.5 lungs showing localization of Fzd6-3xGFP in proximal airways (Ecad), saccules (RAGE and SPC), airway smooth muscle (αSMA), and vasculature (CD31). Scale bars, 10 μm.

(E) Schematic summarizing localization of core PCP proteins in the sacculation-stage lung.

See also Figure S1.

appreciated: at the cellular level, this complex regulates the orientation of airway cilia,[23] and sacculation and alveologenesis are perturbed in PCP-mutant lungs.[12,13,24] However, it is unclear why loss of PCP causes defects in late-stage lung development. Thus, the idea that the PCP complex regulates epithelial widening during sacculation remains an attractive hypothesis.

Please cite this article in press as: Paramore et al., *Vangl*-dependent mesenchymal thinning shapes the distal lung during murine sacculation, Developmental Cell (2024), https://doi.org/10.1016/j.devcel.2024.03.010

Here, we investigated the cellular mechanisms through which the PCP complex influences sacculation. We demonstrate that *Celsr1* is expressed only in the lung epithelium and mesothelium, while *Vangl2* is expressed ubiquitously throughout the lung, including in the pulmonary mesenchyme. We find severe sacculation defects in the lungs of *Vangl2* mutants, but not *Celsr1* mutants. Surprisingly, this phenotype is not reproduced when *Vangl1* and *Vangl2* are depleted from the lung epithelium; instead, sacculation defects arise from loss of *Vangl1/2* in the lung mesenchyme. We also show that loss of mesenchymal *Wnt5a* mimics the sacculation defects observed in *Vangl2*-mutant lungs, implicating *Wnt5a/Vangl* signaling in late-stage embryonic lung development. Using a mathematical model of sacculation, we predict that increasing the fluidity of the mesenchyme increases the extent of epithelial widening. Lineage-labeling experiments and cell-shape analyses suggest that mesenchymal cells actively exchange neighbors during sacculation, and these cellular behaviors are likely perturbed in *Vangl* mutants. Our data thus demonstrate that the pulmonary mesenchyme plays a key, active role in shaping the architecture of the distal lung in a *Vangl*-dependent, *Celsr*-independent manner. These findings add to a growing body of evidence suggesting that PCP genes, whose functions are best understood in planar epithelia, also play important roles in mesenchymal tissues to facilitate morphogenesis.[21,24,25]

RESULTS

Core PCP components are expressed in different patterns during sacculation

To investigate the expression and possible role for PCP components during sacculation, we harvested *E*17.5 lungs from transgenic mice in which endogenous core PCP components are fluorescently tagged, allowing us to assess the localization of Celsr1, Vangl2, and Fzd6 (Figure 1A).[26] We investigated PCP expression across multiple tissues within the lung, including the proximal airways, developing saccules, airway smooth muscle, and vasculature. As expected, Celsr1-3xGFP localizes predominantly to the airway epithelium and is absent from mesenchymal tissues and endothelium (Figure 1B). However, the fluorescence intensity of Celsr1-3xGFP is reduced in the saccular epithelium, suggesting that the expression of Celsr1 might be downregulated in these cells at this stage of development (Figure 1B). Similarly, tdTomato-Vangl2 is highly expressed in the proximal epithelium, with reduced expression in saccules (Figure 1C). Surprisingly, we observe essentially ubiquitous expression of Vangl2 in the pulmonary mesenchyme, where it is membrane-localized in both the airway smooth muscle and the mesenchyme adjacent to saccules (Figure 1C; Figure S1A). Fzd6-3xGFP is expressed at high levels in the proximal epithelium and endothelial cells but appears to be excluded from the airway smooth muscle and saccule-adjacent mesenchyme (Figure 1D).

To assess the expression of the other components of the core PCP complex, we analyzed single-cell RNA sequencing (scRNA-seq) data from *E*17.5 lungs[27] (Figure S1B). Like *Celsr1*, *Celsr2* is only expressed in the epithelium, whereas *Celsr3* is completely absent from the lung at this stage of development (Figure S1C). *Vangl1* is expressed in the same cell populations as *Vangl2*, albeit to a lesser extent (Figure S1D). Finally, *Fzd3* and *Fzd6* are expressed in a small fraction of mesenchymal cells, with higher expression in endothelial, hematopoietic, and epithelial cells (Figure S1E). These data demonstrate that while all core transmembrane PCP components are expressed in the airway epithelium, *Vangl1/2* are enriched in mesenchymal populations in which *Celsr1–3* and *Fzd3/6* are largely absent. Further, *Fzd3/6* are expressed in the pulmonary endothelium independent of *Vangl1/2* and *Celsr1–3*. This compartment-specific expression of different core PCP genes suggests that PCP components may have roles outside of core PCP complex function.

Vangl2$^{Lp/Lp}$ but not *Celsr1*$^{Crsh/Crsh}$ lungs fail to undergo sacculation

To characterize the role of PCP in the formation of saccules, we took advantage of two dominant-negative PCP-mutant mouse strains: the *Celsr1*^{Crsh} and *Vangl2*^{Lp} lines.[19,20] Stable PCP complexes cannot form in embryos homozygous for the *Celsr1*^{Crsh} mutation due to a disruption in Celsr1's cadherin-binding domain, whereas the *Vangl2*^{Lp} mutation impairs trafficking of both Vangl1 and Vangl2 out of the endoplasmic reticulum.[28,29] Homozygosity in either of these alleles leads to loss of PCP function. Initially, we harvested lungs from control and PCP-mutant embryos at *E*18.5 when sacculation is mostly complete. At this stage of development, PCP mutants have complete craniorachischisis (failure to close the neural tube) and severe axis-elongation defects.[19,20] To distinguish between direct effects from loss of PCP and indirect effects from the open neural tube (ONT) and axis-elongation defects, we took advantage of the incomplete penetrance of the ONT phenotype in our *Celsr1*$^{Crsh/Crsh}$ line. Specifically, we compared lungs from ONT *Celsr1*$^{Crsh/Crsh}$ embryos to those that presented with a closed neural tube (CNT), which display no defects in axis elongation (unpublished observations). In wild-type lungs, PCP proteins, including Celsr1, become polarized in the tracheal epithelium beginning at *E*14.5.[23] Despite the CNT phenotype of the *Celsr1*$^{Crsh/Crsh}$ embryos, there is a clear lack of Celsr1 polarization in the tracheas of these animals, indicating loss of PCP function (Figures S2A–S2C). Analysis of *E*18.5 ONT *Celsr1*$^{Crsh/Crsh}$ embryos demonstrated two phenotypically distinct populations: ~40% of the embryos were pink and had blood flow despite the embryonic abnormalities, while the other ~60% were white and appeared to be either dead or dying (Figure S2D). Lung tissue from white *E*18.5 ONT embryos appeared highly abnormal by immunofluorescence (Figure S2E) and so we excluded these samples from our subsequent analysis of ONT *Celsr1*$^{Crsh/Crsh}$ embryos (Figures S2F and S2G).

To quantify the extent of sacculation, we acquired tiled, confocal images of whole lung sections, which enabled us to assess an entire lobe rather than a small sampling of images. We generated a custom sacculation-analysis pipeline to measure both the area of individual saccules and the fractional area of the lung section accounted for by saccules, which we termed "saccule coverage" (Figure 2A). We found that both the saccule coverage and average saccule area are slightly reduced in lungs from ONT *Celsr1*$^{Crsh/Crsh}$ embryos compared with controls at *E*18.5 (Figures 2B–2E). However, we observed no differences between lungs from CNT *Celsr1*$^{Crsh/Crsh}$

Please cite this article in press as: Paramore et al., *Vangl*-dependent mesenchymal thinning shapes the distal lung during murine sacculation, Developmental Cell (2024), https://doi.org/10.1016/j.devcel.2024.03.010

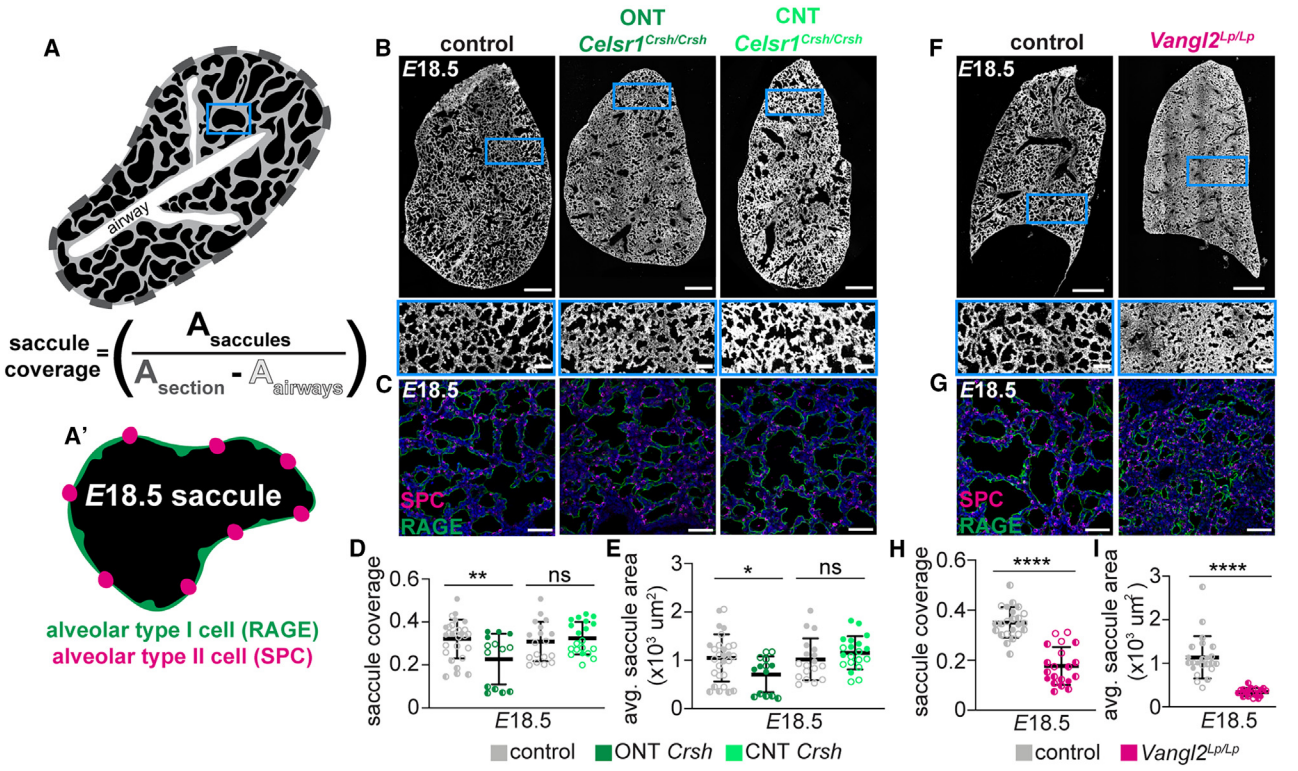

Figure 2. Sacculation fails in *Vangl2*$^{Lp/Lp}$ but not *Celsr1*$^{Crsh/Crsh}$ embryos

(A) Schematic illustrating metric used to quantify saccule coverage, where A denotes area; A′, Illustration of an *E*18.5 saccule and the marker proteins used to identify AEC1s and AEC2s.

(B) Representative tiled images (scale bars, 500 μm) and insets (scale bars, 100 μm) of *E*18.5 lung sections from control, ONT, and CNT *Celsr1*$^{Crsh/Crsh}$ lungs; fluorescence intensity includes signal from staining for SPC, RAGE, and Hoechst.

(C) Representative images of sections of distal lung tissue at *E*18.5 in control, ONT *Celsr1*$^{Crsh/Crsh}$, and CNT *Celsr1*$^{Crsh/Crsh}$ lungs; scale bars, 50 μm.

(D) Quantification of the percentage of lung area accounted for by saccules at *E*18.5 in control, ONT *Celsr1*$^{Crsh/Crsh}$ (n = 6 control and n = 3 mutant lungs, p = 0.0066 via unpaired Student's t test), and CNT *Celsr1*$^{Crsh/Crsh}$ lungs (n = 4 control and n = 4 mutant lungs, p = 0.5795 via unpaired Student's t test); each data point is one lung lobe.

(E) Quantification of average saccular lumenal area at *E*18.5 in control, ONT *Celsr1*$^{Crsh/Crsh}$ (n = 6 control and n = 3 mutant lungs, p = 0.0271 via unpaired Student's t test), and CNT *Celsr1*$^{Crsh/Crsh}$ lungs (n = 4 control and n = 4 mutant lungs, p = 0.2918 via unpaired Student's t test); each data point is one lung lobe.

(F) Representative tiled images (scale bars, 500 μm) and insets (scale bars, 100 μm) of *E*18.5 lung sections from control and *Vangl2*$^{Lp/Lp}$ lungs; fluorescence intensity includes signal from staining for SPC, RAGE, and Hoechst.

(G) Representative images of sections of distal lung tissue at *E*18.5 in control and *Vangl2*$^{Lp/Lp}$ lungs; scale bars, 50 μm.

(H) Quantification of the percentage of lung area accounted for by saccules at *E*18.5 in control and *Vangl2*$^{Lp/Lp}$ lungs (n = 6 control and n = 5 mutant lungs, p < 0.0001 via unpaired Student's t test); each data point is one lung lobe.

(I) Quantification of average saccular lumenal area at *E*18.5 in control and *Vangl2*$^{Lp/Lp}$ lungs (n = 6 control and n = 5 mutant lungs, p < 0.0001 via unpaired Student's t test); each data point is one lung lobe. Shown are mean ± SD; * p < 0.05; ** p < 0.01; **** p < 0.0001. In all graphs, different shapes represent distinct experimental replicates.

See also Figure S2.

embryos and controls (Figures 2B–2E). Furthermore, CNT *Celsr1*$^{Crsh/Crsh}$ pups are viable and can breathe after birth, consistent with these animals achieving normal sacculation. These data suggest that the slight reduction in sacculation observed in the ONT *Celsr1*$^{Crsh/Crsh}$ embryos is a consequence of gross abnormalities of the embryo rather than due to loss of *Celsr1* in the lung per se. In contrast, *Vangl2*$^{Lp/Lp}$ lungs exhibit severe sacculation defects (Figures 2F and 2G). At *E*18.5, *Vangl2*$^{Lp/Lp}$ lungs have significantly reduced saccule coverage compared with controls (Figure 2H) and significantly smaller saccule areas (Figure 2I). Thus, our data demonstrate a role for *Vangl*, but not *Celsr*, in regulating sacculation of the embryonic mouse lung.

Vangl1/2 is required in the mesenchyme for sacculation

Because *Vangl1/2* are expressed in both mesenchymal and epithelial compartments during sacculation, we took advantage of tissue-specific knockouts to determine whether sacculation requires *Vangl1/2* in the epithelium, the mesenchyme, or both. We generated *ShhCre*; *Vangl1*$^{fl/fl}$; *Vangl2*$^{fl/fl}$ (epiCKO) embryos, which have conditional deletion of *Vangl1/2* in the airway epithelium and show loss of PCP asymmetry (Figures S3A–S3D). We also generated *Dermo1Cre*; *Vangl1*$^{fl/fl}$; *Vangl2*$^{fl/fl}$ (mesCKO) embryos in which broad expression of *Cre* in the splanchnic mesoderm leads to conditional deletion of *Vangl1/2* from the pulmonary mesenchyme but not the epithelium (Figure S3E).[30,31] Of note, the *Dermo1Cre* allele and the *Vangl2*

Please cite this article in press as: Paramore et al., *Vangl*-dependent mesenchymal thinning shapes the distal lung during murine sacculation, Developmental Cell (2024), https://doi.org/10.1016/j.devcel.2024.03.010

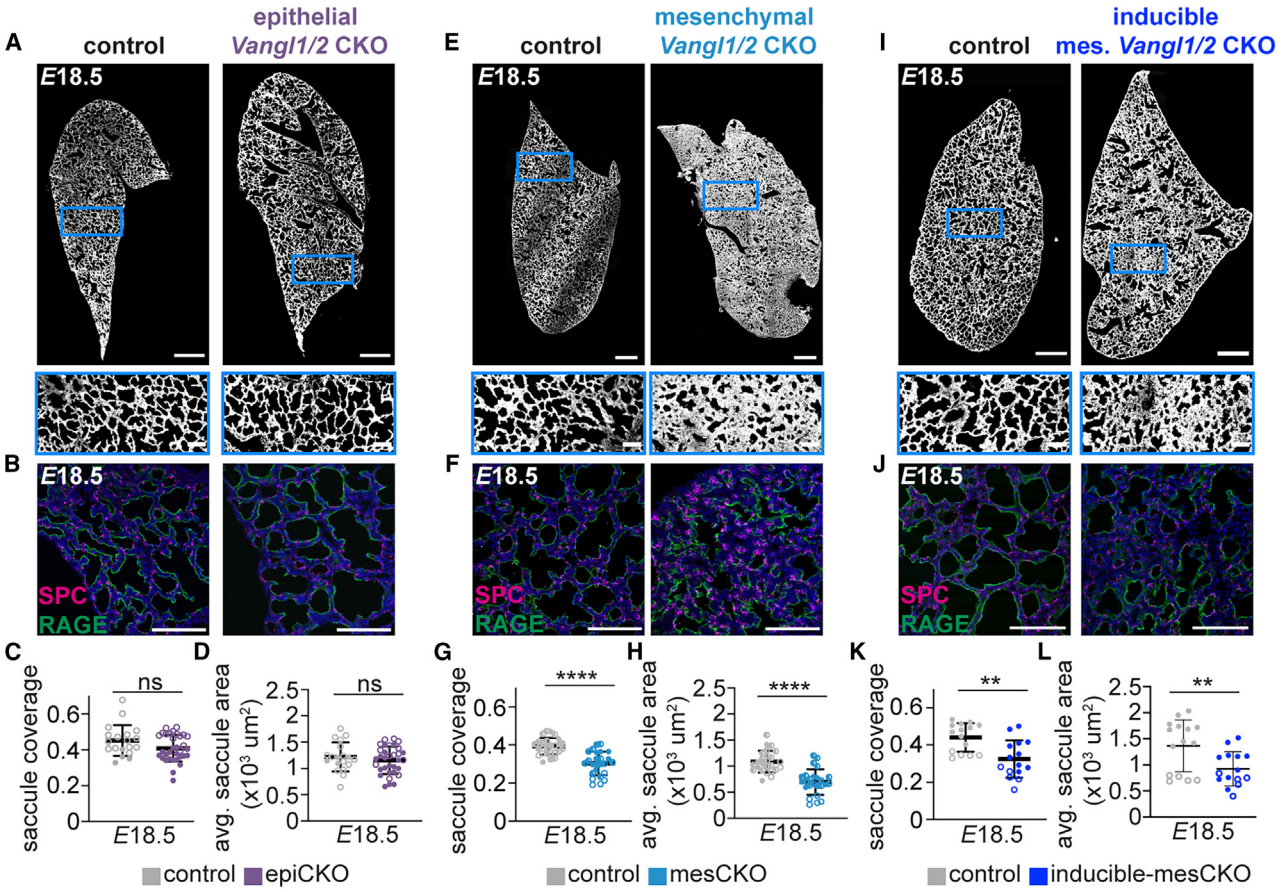

Figure 3. Sacculation requires *Vangl1/2* in the pulmonary mesenchyme but not the airway epithelium

(A) Representative tiled images (scale bars, 500 μm) and insets (scale bars, 100 μm) of *E*18.5 lung sections from control and epiCKO lungs; fluorescence intensity includes signal from staining for RAGE and Hoechst and transgenic mTmG fluorescence.

(B) Representative images of sections of distal lung tissue at *E*18.5 in control and epiCKO lungs; scale bars, 100 μm.

(C) Quantification of the percentage of lung area accounted for by saccules at *E*18.5 in control and epiCKO lungs (n = 4 control and n = 7 mutant lungs, p = 0.0620 via unpaired Student's t test); each data point represents one lung lobe.

(D) Quantification of average saccular lumenal area at *E*18.5 in control and epiCKO lungs (n = 4 control and n = 7 mutant lungs, p = 0.4020 via unpaired Student's t test); each data point represents one lung lobe.

(E) Representative tiled images (scale bars, 500 μm) and insets (scale bars, 100 μm) of *E*18.5 lung sections from control and mesCKO lungs; fluorescence intensity includes signal from staining for RAGE and Hoechst and transgenic mTmG fluorescence.

(F) Representative images of sections of distal lung tissue at *E*18.5 in control and mesCKO lungs; scale bars, 100 μm.

(G) Quantification of the percentage of lung area accounted for by saccules at *E*18.5 in control and mesCKO lungs (n = 5 control and n = 5 mutant lungs, p < 0.0001 via unpaired Student's t test); each data point represents one lung lobe.

(H) Quantification of average saccular lumenal area at *E*18.5 in control and mesCKO lungs (n = 5 control and n = 5 mutant lungs, p < 0.0001 via unpaired Student's t test); each data point represents one lung lobe.

(I) Representative tiled images (scale bars, 500 μm) and insets (scale bars, 100 μm) of *E*18.5 lung sections from control and inducible-mesCKO lungs; fluorescence intensity includes staining for RAGE and Hoechst and transgenic mTmG fluorescence.

(J) Representative images of sections of distal lung tissue at *E*18.5 in control and inducible-mesCKO lungs; scale bars, 100 μm.

(K) Quantification of the percentage of lung area accounted for by saccules at *E*18.5 in control and inducible-mesCKO lungs (n = 3 control and n = 3 mutant lungs, p = 0.0013 via unpaired Student's t test); each data point represents one lung lobe.

(L) Quantification of average saccular lumenal area at *E*18.5 in control and inducible-mesCKO lungs (n = 3 control and n = 3 mutant lungs, p = 0.0076 via unpaired Student's t test); each data point represents one lung lobe. Shown are mean ± SD; ** p < 0.01; **** p < 0.0001. In all graphs, different shapes represent distinct experimental replicates.

See also Figure S3.

gene both reside on chromosome 1, so generating *Dermo1Cre; Vangl2*$^{fl/fl}$ embryos required meiotic recombination between the *Vangl2* locus and the *Dermo1Cre* insertion site. As expected, mesenchymal loss of *Vangl1/2* does not affect Celsr1 polarity in the tracheal epithelium, indicating that the PCP complex is functional in the epithelium in the mesCKO embryos (Figures S3F and S3G).

We found that epiCKO lungs undergo sacculation and are indistinguishable from controls at *E*18.5 (Figures 3A–3D). In contrast, mesCKO lungs exhibit sacculation defects similar

Please cite this article in press as: Paramore et al., *Vangl*-dependent mesenchymal thinning shapes the distal lung during murine sacculation, Developmental Cell (2024), https://doi.org/10.1016/j.devcel.2024.03.010

to those observed in *Vangl2*$^{Lp/Lp}$ lungs, with significantly reduced saccule coverage, smaller saccular areas, and a thicker mesenchyme (Figures 3E–3H). Further, these defects in saccule formation were associated with alterations in the proportions of AEC populations: mesCKO lungs exhibit a slight but significant decrease in the fraction of AEC2s (Figure S3H). To confirm that *Vangl1/2* are specifically required in the pulmonary mesenchyme during sacculation, we generated a second mesenchymal knockout line with an inducible *Cre* (*Tbx4-rtTA; Tet-O-Cre; Vangl1*$^{fl/fl}$; *Vangl2*$^{fl/fl}$; inducible-mesCKO) in which *Cre* expression is restricted to the pulmonary mesenchyme.[32] We introduced doxycycline via drinking water and intraperitoneal injection at *E*14.5 to ensure loss of Vangl1/2 protein by *E*16.5, as Vangl2 can remain stable at the membrane for more than a day (unpublished observations). We found that inducible-mesCKO lungs have sacculation defects at *E*18.5, phenocopying both the *Vangl2*$^{Lp/Lp}$ and mesCKO animals (Figures 3I–3L). Notably, if a single functional allele of *Vangl1* or *Vangl2* remained in the embryo (i.e., *Vangl1*$^{fl/+}$; *Vangl2*$^{fl/fl}$ or *Vangl1*$^{fl/fl}$; *Vangl2*$^{fl/+}$), no defects were observed and mice were viable postnatally; thus, *Vangl1* and *Vangl2* compensate for each other in this tissue. To determine whether the sacculation defects are caused by changes in cell proliferation or apoptosis, we performed immunofluorescence analysis for phospho-histone-3 and cleaved caspase-3 on control and mesCKO lungs at *E*16.5–18.5. We found no differences in proliferation or apoptosis between controls and mutants (Figures S3I–S3L). Altogether, these data suggest that the sacculation defects observed in *Vangl2*$^{Lp/Lp}$ embryos are a consequence of a loss of *Vangl* function specifically in the pulmonary mesenchyme during sacculation rather than due to a requirement for *Vangl* or the PCP complex in the lung epithelium.

Loss of Wnt5a in the pulmonary mesenchyme mimics loss of mesenchymal Vangl1/2

In epithelia, Vangl2 functions in concert with Celsr1 to affect diverse outcomes, ranging from convergent extension to oriented ciliogenesis.[23,29,33–38] In the pulmonary mesenchyme, however, our data show that Vangl2 acts independently of Celsr1 to promote sacculation. Outside of its core PCP-binding partners, *Vangl2* has been reported to physically or genetically interact with non-canonical Wnt receptor tyrosine kinases, including *Ror2*, *Ptk7*, and *Ryk*.[39–41] Analysis of scRNA-seq data from *E*17.5 lungs[27] showed that *Ror2*, *Ptk7*, and *Ryk* are all expressed in the mesenchyme (Figure 4A; Figure S1A). Of these receptors, *Ryk* shows the strongest expression in the lung during this developmental period, with highest expression in the lung mesenchyme. Each of these receptors has been hypothesized or shown to function downstream of Wnt5a, a non-canonical Wnt ligand.[41–43] Consistently, the scRNA-seq analysis also shows that *Wnt5a* is expressed predominantly in the lung mesenchyme at *E*17.5 and at lower levels in the epithelium (Figure 4A). In many developmental contexts, including tracheal morphogenesis and alveologenesis, a *Wnt5a/Ror2/Vangl* signaling pathway has been implicated in mesenchymal cell polarization and migration.[24,41,42,44] Given that embryo-wide loss of *Wnt5a* immediately prior to sacculation phenocopies the defects observed in our *Vangl1/2* mesCKO lungs,[42] we hypothesized that *Wnt5a* may be upstream of *Vangl* function in the sacculating lung.

To determine whether Wnt5a could play a role in Vangl1/2-mediated epithelial expansion and mesenchymal thinning, we generated epithelial (*ShhCre; Wnt5a*$^{fl/fl}$) and inducible-mesenchymal (*Tbx4-rtTA*; *Tet-O-Cre*; *Wnt5a*$^{fl/fl}$) *Wnt5a*-knockout embryos. Surprisingly, we found that loss of *Wnt5a* in the lung epithelium has no effect on sacculation (Figures 4B–4E). In contrast, inducible deletion of *Wnt5a* from the pulmonary mesenchyme at *E*15.5 results in sacculation defects that phenocopy loss of mesenchymal *Vangl1/2* (Figures 4F–4I). Examination of mesenchymal Vangl2 in lungs from inducible-mesenchymal *Wnt5a*-knockout embryos revealed no significant difference in Vangl2 fluorescence intensity or changes in membrane localization (Figures S4A and S4B). Potentially, this may indicate that Wnt5a regulates Vangl2 at the post-translational level, similar to its role in the limb.[41] We thus hypothesize that Wnt5a may be part of a signaling pathway through which Vangl functions in contexts where Celsr is absent.

Mathematical modeling predicts a role for mesenchymal cell rearrangements during sacculation

Our observation that Vangl is required in the mesenchyme for sacculation was surprising, as the nonplanar organization of mesenchymal cells is inconsistent with any obvious axis of planar polarization. As a part of its role in the PCP complex, Vangl promotes the asymmetric localization of cytoskeletal components, leading to collective cell movements such as convergent extension; in the absence of Vangl, the cytoskeletal rearrangements that generate epithelial neighbor exchanges are lost, and cells remain in place.[20,21,45–48] At earlier stages of development, time-lapse imaging analysis has demonstrated that the pulmonary mesenchyme is a highly motile and fluid tissue.[49] Thus, we hypothesized that the mesenchyme might be similarly fluid during sacculation and that the ability of mesenchymal cells to exchange neighbors might depend on expression of Vangl.

Because of its size, geometry, and need for blood flow and lumenal pressure, time-lapse imaging of the late-stage embryonic mouse lung remains technically challenging. Therefore, to test the validity of our hypothesis, we turned to mathematical modeling. This approach allowed us to determine the relative roles of mesenchymal fluidity and other known mechanical forces during sacculation. In the model, the epithelial layer consists of chains of cells represented as a curved line, simulating two-dimensional (2D) saccules. The epithelial cells experience cell-cell interactions as well as outward movements due to lumenal pressure. The epithelium exhibits a "bending elasticity," which allows it to change shape in response to forces from the pressure within the lumen (Figure 5A).[9,50,51] We approximated the mesenchyme as a packed field of cells; the ability of the cells within this tissue to exchange neighbors depends on its relative fluidity, which is related to both mesenchymal cell motility (specified by a polarity term) and the forces of cell-cell interactions (specified by a mobility term [inverse of the friction parameter]). The model also specifies the (indirect) interactions between the epithelial monolayer and surrounding mesenchymal cells, such that deformation of the epithelium is

Please cite this article in press as: Paramore et al., *Vangl*-dependent mesenchymal thinning shapes the distal lung during murine sacculation, Developmental Cell (2024), https://doi.org/10.1016/j.devcel.2024.03.010

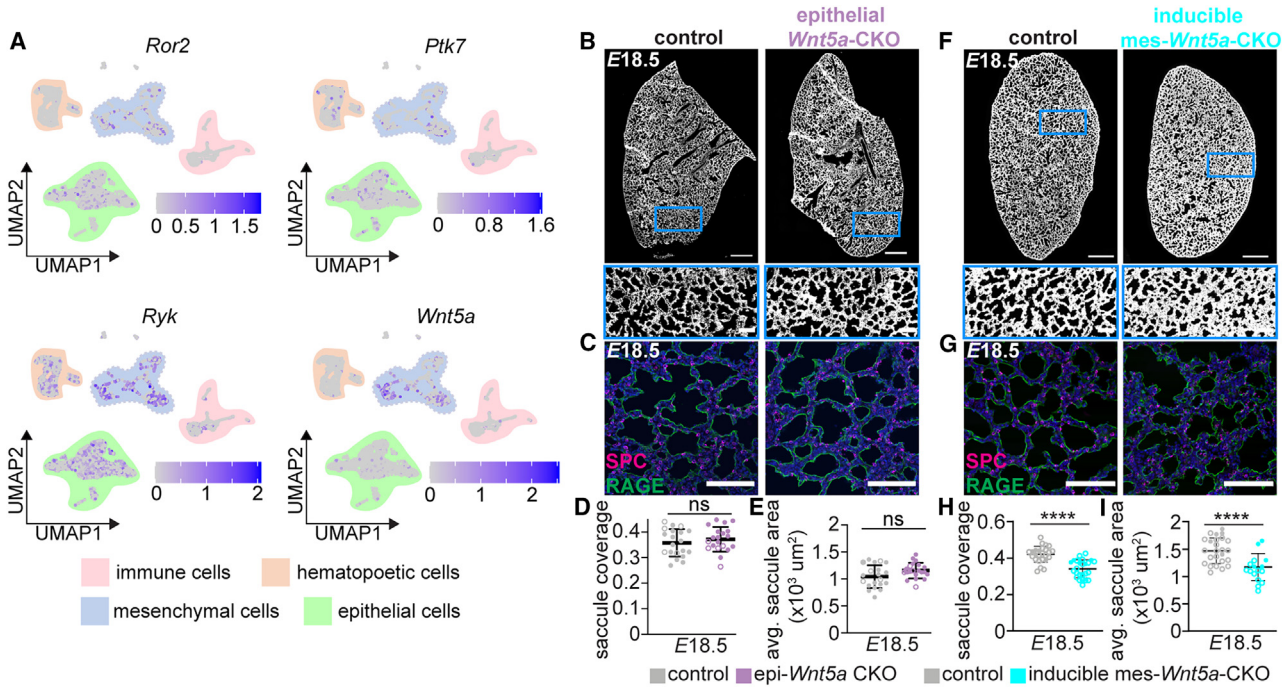

Figure 4. Loss of mesenchymal Wnt5a mimics loss of Vangl1/2 during sacculation

(A) scRNA-seq analysis of *E*17.5 lungs; data from Zepp et al.[27] Cells are clustered into four main groups: immune, epithelial, hematopoietic, and mesenchymal cells. UMAP projections show the relative expression of *Ror2*, *Ptk7*, *Ryk*, and *Wnt5a*.

(B) Representative tiled images (scale bars, 500 μm) and insets (scale bars, 100 μm) of *E*18.5 lung sections from control and epi-*Wnt5a*-CKO lungs; fluorescence intensity includes signal from staining for SPC, RAGE, and Hoechst.

(C) Representative images of sections of distal lung tissue at *E*18.5 in control and epi-*Wnt5a*-CKO lungs; scale bars, 100 μm.

(D) Quantification of the percentage of lung area accounted for by saccules at *E*18.5 in control and epi-*Wnt5a*-CKO lungs (n = 4 control and n = 4 mutant lungs, p = 0.3994 via unpaired Student's t test); each data point represents one lung lobe.

(E) Quantification of average saccular lumenal area at *E*18.5 in control and epi-*Wnt5a*-CKO lungs (n = 4 control and n = 4 mutant lungs, p = 0.0552 via unpaired Student's t test); each data point represents one lung lobe.

(F) Representative tiled images (scale bars, 500 μm) and insets (scale bars, 100 μm) of *E*18.5 lung sections from control and inducible mes-*Wnt5a*-CKO lungs; fluorescence intensity includes signal from staining for SPC, RAGE, and Hoechst.

(G) Representative images of sections of distal lung tissue at *E*18.5 in control and inducible mes-*Wnt5a*-CKO lungs; scale bars, 100 μm.

(H) Quantification of the percentage of lung area accounted for by saccules at *E*18.5 in inducible mes-*Wnt5a*-CKO lungs (n = 5 control and n = 5 mutant lungs, p < 0.0001 via unpaired Student's t test); each data point represents one lung lobe.

(I) Quantification of average saccular lumenal area at *E*18.5 in control and inducible mes-*Wnt5a*-CKO lungs (n = 5 control and n = 5 mutant lungs, p < 0.0001 via unpaired Student's t test); each data point represents one lung lobe. Shown are mean ± SD; **** p < 0.0001. In all graphs, different shapes represent distinct experimental replicates.

See also Figure S4.

coupled to rearrangements in the mesenchyme. The initial size and density of the saccules and the density of the mesenchymal cells were based on data collected from *E*16.5 wild-type lungs (Figures S5A–S5F).

Because previous work has suggested that mechanical forces from fluid pressure are required for sacculation to proceed, we independently varied two parameters in the model: lumenal pressure and mesenchymal fluidity. We found that when lumenal pressure is low, the epithelium fails to expand, regardless of the fluidity of the mesenchyme (Figures 5Bi, 5Bii, S5G, and S5H; Videos S1 and S2). When both lumenal pressure and mesenchymal fluidity are high, the mesenchyme between adjacent epithelial compartments thins and the simulated epithelium expands into saccules (Figure 5Biii; Video S3). However, when lumenal pressure is high and mesenchymal fluidity is low, the mesenchyme remains thick, and expansion of the epithelium is constrained (Figure 5Biv; Video S4).

We found that under high-pressure, high-fluidity conditions, sacculation *in silico* proceeds similarly to sacculation *in vivo* in wild-type lungs (Figure 5C). The mesenchymal layer between epithelial compartments is thinner at the final time point of the simulation than at the initial time point, similar to the changes in mesenchymal thickness observed *in vivo* from *E*16.5–18.5. Importantly, simulations in which pressure is high but fluidity is low result in smaller saccules and a thicker mesenchyme, consistent with the morphological defects that we observe when *Vangl1/2* is depleted from the mesenchyme *in vivo* (Figure 5D). Consistently, decreasing the fluidity of the mesenchyme decreases the average saccule area in the simulation, even when the lumenal pressure is high (Figure 5E). Our model therefore predicts that lumenal pressure and a fluid mesenchyme are both essential for sacculation and that loss of either leads to failure in this morphogenetic process.

Please cite this article in press as: Paramore et al., *Vangl*-dependent mesenchymal thinning shapes the distal lung during murine sacculation, Developmental Cell (2024), https://doi.org/10.1016/j.devcel.2024.03.010

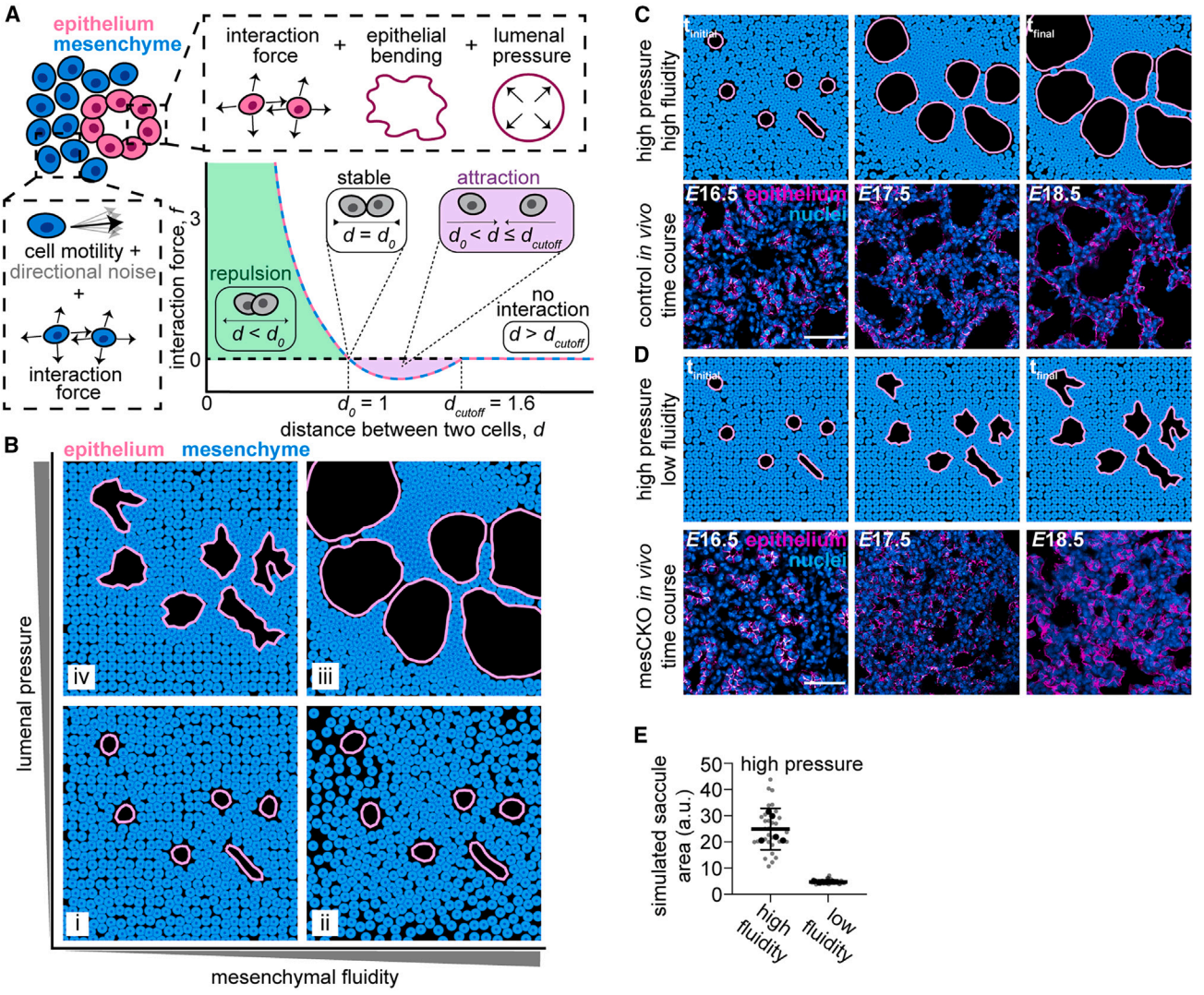

Figure 5. Mathematical modeling predicts that sacculation requires fluidity of the mesenchyme

(A) Schematic of the parameters used to model the epithelium and mesenchyme.

(B) Phase diagram of final time point of simulations that independently vary lumenal fluid pressure and mesenchymal fluidity.

(C) Snapshots of the time course of sacculation in high-pressure, high-fluidity simulations and in wild-type lungs *in vivo*. Images of *E*16.5–17.5 lung sections immunostained for Ecad (magenta) and counterstained with Hoechst (cyan); *E*18.5 lung sections immunostained for RAGE and SPC (both magenta), counterstained with Hoechst (cyan) (scale bars, 50 μm).

(D) Snapshots of the time course of sacculation in high-pressure, low-fluidity simulations and in mesCKO lungs. Images of *E*16.5–17.5 lung sections immunostained for Ecad (magenta), counterstained with Hoechst (cyan); *E*18.5 lung sections immunostained for RAGE and SPC (both magenta), counterstained with Hoechst (cyan) (scale bars, 50 μm).

(E) Quantification of the average saccule area at the final time point of high-pressure, high-fluidity and high-pressure, low-fluidity simulations.

See also Videos S1, S2, S3, and S4 and Figure S5.

Lineage tracing identifies a fluid mesenchymal cell compartment

Our mathematical model predicts that a fluid mesenchymal compartment is required for epithelial expansion and mesenchymal thinning during sacculation. Our model also predicts that this fluidity results in both active rearrangements of neighboring mesenchymal cells as well as dispersal of cells during the process of sacculation (Figures 6A–6C). To test this prediction experimentally, we used the *Confetti* lineage-tracing system to assess the extent to which mesenchymal cells disperse during sacculation. We generated *Tbx4-rtTA*; *Tet-O-Cre*; *Confetti* mice to lineage label individual mesenchymal cells and follow their progeny through developmental time. In this system, exposure to doxycycline promotes the random expression of one of four fluorophores in a subset of cells within the pulmonary mesenchyme. After injecting a single low dose of doxycycline at *E*14.5, we observed extremely rare groups of GFP^+ clonal populations at *E*16.5 (Figure 6D). To assess the extent to which mesenchymal cells disperse during sacculation, we conducted an experimental time course from *E*16.5–18.5 (Figure 6D). We

Please cite this article in press as: Paramore et al., *Vangl*-dependent mesenchymal thinning shapes the distal lung during murine sacculation, Developmental Cell (2024), https://doi.org/10.1016/j.devcel.2024.03.010

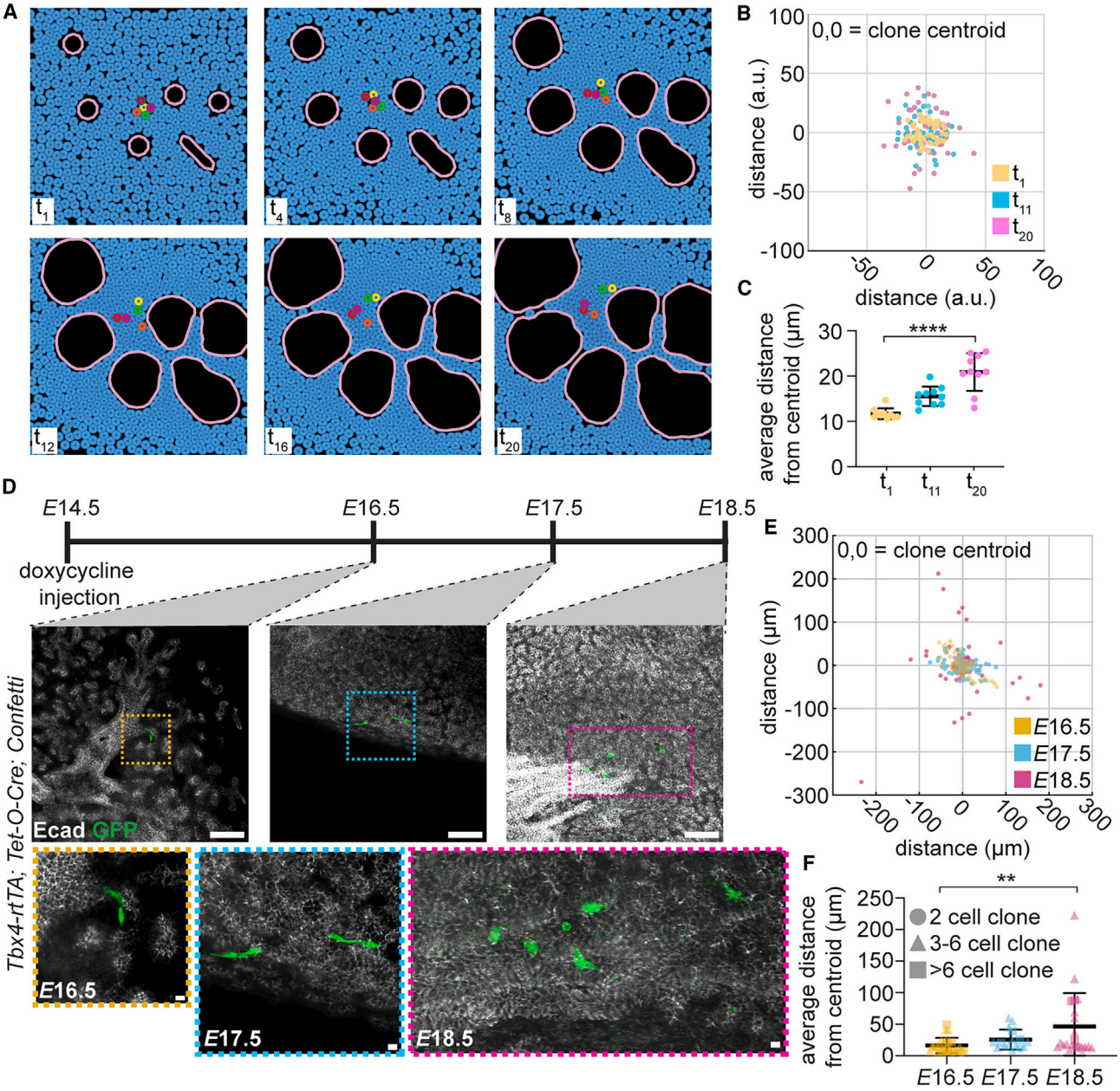

Figure 6. Lineage tracing demonstrates a fluid mesenchymal compartment

(A) Snapshots of the time course of sacculation in high-pressure, high-fluidity simulation, with mesenchymal cells color-coded to highlight neighbor exchanges.

(B) Graphical representation of clonal cell positions at t_1–t_{20} in high-pressure, high-fluidity simulations; 0,0 is the centroid of each clone. Each dot represents one cell; ten simulations are represented.

(C) Graph indicating the average distance of daughter cells from the centroid of their clonal population at t_1–t_{20} in high-pressure, high-fluidity simulations; each dot represents the average distance of all daughter cells from the centroid in one simulation (n = 10 simulations, $p < 0.0001$ via unpaired Student's t test).

(D) Schematic illustrating experimental protocol for inducing sparse clonal populations, including representative images of clones from 300-μm-thick sections of *Tbx4-rtTA; Tet-O-Cre; Confetti* lungs at *E*16.5–18.5 (scale bars, 100 μm; inset scale bars, 10 μm).

(E) Graphical representation of clonal cell positions at *E*16.5–18.5 in control lungs; 0,0 is the centroid of each clone. Each dot represents one cell (n = 19 clones from 6 distinct *E*16.5 lungs, n = 6 clones from 4 distinct *E*17.5 lungs, and n = 19 clones from 5 distinct *E*18.5 lungs).

(F) Graph indicating the average distance of daughter cells from the centroid of their clonal population at *E*16.5–18.5 in control lungs (n = 19 clones from 6 distinct *E*16.5 lungs, n = 6 clones from 4 distinct *E*17.5 lungs, and n = 19 clones from 5 distinct *E*18.5 lungs, $p = 0.0039$ via Mann-Whitney test comparing E16.5 and E18.5).

See also Figure S6.

Please cite this article in press as: Paramore et al., *Vangl*-dependent mesenchymal thinning shapes the distal lung during murine sacculation, Developmental Cell (2024), https://doi.org/10.1016/j.devcel.2024.03.010

then determined the centroid position of each clonal population and plotted the coordinates of all clonal cells with the centroid as the origin (Figure 6E; Figures S6A–S6C). Although the median number of cells per clone was 4 at both stages, cells in clones at *E*18.5 appeared much further apart than those at *E*16.5, consistent with mesenchymal cell dispersal and a fluid compartment (Figure 6E; Figure S6D). Measuring the average distance of sister cells from the centroid of each clonal population demonstrated that cells disperse over developmental time, consistent with the predictions of our mathematical model (Figure 6F).

Because our lineage-labeling strategy generated mesenchymal clones both proximal and distal to the conducting airways, we asked whether there were location-dependent differences in dispersal of the clones. Analysis of clonal dispersion from *E*16.5–18.5 identified no obvious trends in the levels of dispersal as a function of distance from the conducting airways (Figures S6E–S6H). Given that clone dispersion does not strongly correlate with anatomical location, we conclude that mesenchymal cells throughout the lung are broadly capable of dispersal. Together, our data indicate that the mesenchyme of the sacculation-stage lung is fluid. We hypothesize that this fluidity is necessary for mesenchymal thinning and the increase in epithelial surface area during sacculation.

Vangl-mutant mesenchymal cells exhibit cell morphologies inconsistent with a fluid compartment

Our lineage-tracing data are consistent with our mathematical model, which predicts that the mesenchyme is a fluid compartment during sacculation. We previously found that the fluidity of the mesenchymal compartment correlates with elongated and protrusive cell shapes in early-stage lungs more amenable to time-lapse imaging analysis.[49,52] We therefore hypothesized that, if the saccular mesenchyme is a fluid tissue, the morphology of mesenchymal cells would be similarly elongated at the sacculation stage in wild-type lungs.

To test this hypothesis, we used a *Tbx4-rtTA*; *Tet-O-Cre*; *Confetti* mouse line and induced labeling of mesenchymal cells at *E*14.5, which ensures that no pulmonary endothelial cells are labeled.[32] By performing immunofluorescence analysis for Ecad, we ensured that only images of saccule-associated mesenchymal cells were obtained, avoiding airway and vascular smooth muscle. We then examined the shapes of saccule-associated mesenchymal cells at *E*17.5. Near the saccules, mesenchymal cells exhibit an elongated morphology, often wrapping around the epithelium (Figure 7A). This elongated morphology is consistent with cell shapes observed in fluid or motile tissue compartments.[49,52] To determine whether the morphology of mesenchymal cells is altered when *Vangl1/2* are depleted, we introduced the *Confetti* allele into our inducible mesenchymal *Vangl1/2* knockout line (*Tbx4-rtTA*; *Tet-O-Cre*; $Vangl1^{fl/fl}$; $Vangl2^{fl/fl}$; *Confetti*), where any cell expressing a Confetti fluorophore will also be mutant for *Vangl1/2*. Unlike cells from control embryos, *Vangl1/2*-mutant mesenchymal cells adjacent to saccules appear less elongated and less protrusive, resembling blocks (Figure 7B). To quantitatively describe these changes in cell morphology, we performed automated segmentation of Confetti-labeled mesenchymal cells and analyzed four different shape metrics: aspect ratio, shape factor, circularity, and the ratio of cell area to the area of its convex hull. These cell-shape analyses showed that the *Vangl1/2*-mutant cells significantly differed from control cells in their morphology: mutant cells have an increased circularity, a reduced aspect ratio, a lower shape factor, and a higher ratio of area to convex hull area (Figures 7C–7F), morphologies that are consistent with a less fluid or motile state. These data indicate that loss of *Vangl* alters mesenchymal cell morphology, which is consistent with our predictions of a less fluid compartment.

DISCUSSION

Sacculation is an integral part of embryonic development, generating the epithelial surface area required for gas exchange postnatally. However, we still know relatively little about the cellular mechanisms underlying this developmental process. Our data demonstrate that neither *Vangl1/2* nor *Celsr1*, core members of the PCP complex, are necessary in the pulmonary epithelium for sacculation. Rather, *Vangl1/2* function is required in the mesenchyme for mesenchymal thinning and epithelial expansion, key morphogenetic events that drive sacculation. Thus, we have identified a PCP-independent role for Vangl, where it functions without its cognate partner Celsr to promote morphogenesis.

Our findings indicate that Vangl may be part of a signaling pathway downstream of Wnt5a, which is considered a non-canonical Wnt ligand that predominantly functions independently of β-catenin.[53] In general, loss of *Wnt5a* affects morphogenesis of tissues rather than altering cell identity or specification.[53] Given the phenotypic similarities in *Wnt5a*-mutant and *Vangl2*-mutant embryos, it has long been hypothesized that Wnt5a is an upstream regulator of core PCP complex function. However, our data suggest that, instead, Wnt5a may signal to Vangl in its PCP-independent roles. Future studies are required to identify a Wnt5a receptor, and to determine the molecular relay downstream of Wnt5a that may lead to Vangl activation in the pulmonary mesenchyme.

Our data are consistent with previous reports of a sacculation defect in the lungs of $Vangl2^{Lp/Lp}$ mutants.[13] In contrast to that work, however, we found that most $Celsr1^{Crsh/Crsh}$ mutant lungs sacculate normally. Because we only observe sacculation defects in lungs of the most phenotypically abnormal $Celsr1^{Crsh/Crsh}$ embryos, we postulate that the previously reported sacculation defects in $Celsr1^{Crsh/Crsh}$ embryos are secondary to defects in the vascular system or embryonic demise. These data highlight the need for caution in interpreting genetic manipulations that also affect the gross morphology and viability of the embryo.

Our data are in apparent conflict with a previous report, which concluded that the core PCP complex is required in the pulmonary epithelium for normal alveolar development.[24] Specifically, the authors of that study used *Sox9Cre* to drive deletion of *Vangl1* and *Vangl2*, which led to a disruption in alveologenesis. However, *Sox9Cre* is not an epithelial-specific driver in the lung; in fact, Sox9 is expressed broadly in the developing pulmonary mesenchyme, including prechondrocytes and mesenchymal cells adjacent to airways.[54] The authors also conducted similar experiments with the *ShhCre* driver but found no alveologenesis defects and attributed this to inefficient depletion of Vangl2 by *ShhCre*. In our hands, we observe complete loss of Vangl2 protein with the *ShhCre* driver (Figure S3A). Further,

Please cite this article in press as: Paramore et al., *Vangl*-dependent mesenchymal thinning shapes the distal lung during murine sacculation, Developmental Cell (2024), https://doi.org/10.1016/j.devcel.2024.03.010

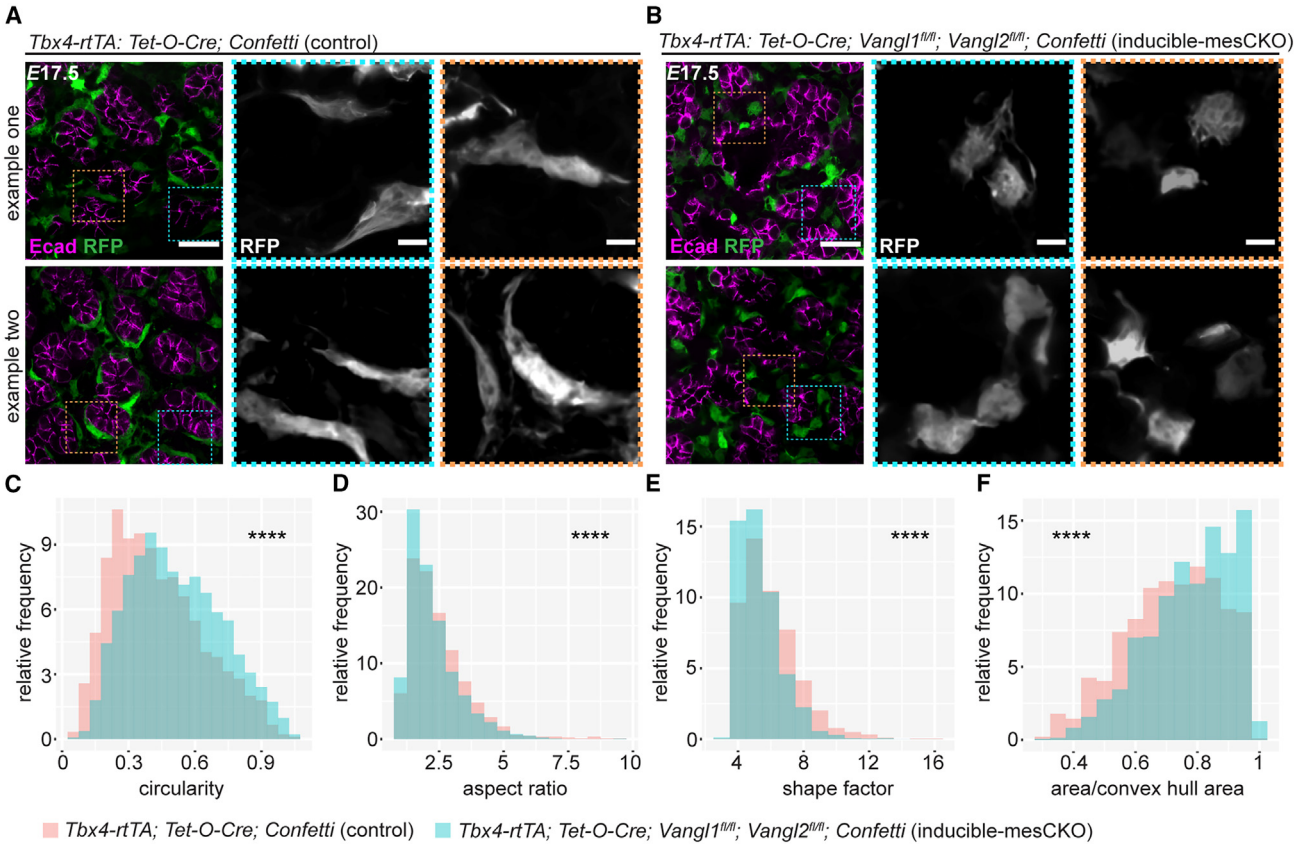

Figure 7. *Vangl2*-mutant mesenchymal cells exhibit altered morphologies

(A) Representative optical sections from two separate *E*17.5 *Tbx4-rtTA; Tet-O-Cre; Confetti* lung lobes. 200-μm-thick sections were immunostained for Ecad (magenta) and imaged for RFP fluorescence (green) (scale bars, 25 μm; inset scale bars, 5 μm).

(B) Representative optical sections from two separate *E*17.5 *Tbx4-rtTA*; *Tet-O-Cre*; *Vangl1*$^{fl/fl}$; *Vangl2*$^{fl/fl}$; *Confetti* lung lobes. 200-μm-thick sections were immunostained for Ecad (magenta) and imaged for RFP fluorescence (green) (scale bars, 25 μm; inset scale bars, 5 μm).

(C–F) Histograms of quantification for the circularity ($p < 2.2e{-}16$, Wilcoxon rank-sum test), aspect ratio ($p = 5.953e{-}07$, Wilcoxon rank-sum test), shape factor ($p < 2.2e{-}16$, Wilcoxon rank-sum test), and area/convex hull area ($p < 2.2e{-}16$, Wilcoxon rank-sum test) of mesenchymal cells from *E*17.5 *Tbx4-rtTA*; *Tet-O-Cre*; *Confetti* (n = 894 cells from 4 lungs) and *Tbx4-rtTA*; *Tet-O-Cre*; *Vangl1*$^{fl/fl}$; *Vangl2*$^{fl/fl}$; *Confetti* lungs (n = 1,330 cells from 3 lungs).

epithelial-specific loss of PCP function in the lung is compatible with survival: *ShhCre; Vangl1/2*$^{fl/fl}$ mice, CNT *Celsr1*$^{Crsh/Crsh}$ mice, *Celsr1*$^{KO/KO}$ mice,[55] and *Celsr2*$^{KO/KO}$ mice[55] can all survive to adulthood, indicating functional lungs. All together, these data suggest that the phenotype of the *Sox9Cre*; *Vangl1/2*$^{fl/fl}$ mice is due to a loss of *Vangl1/2* from the mesenchyme, not the lung epithelium. This conclusion is consistent with the phenotypes of our epithelial- and mesenchymal-specific knockouts of *Vangl1/2*, which clearly demonstrate that Vangl1/2, and the core PCP complex more broadly, are not required in the pulmonary epithelium for lung morphogenesis. Rather, it appears that the main morphogenetic role for the core PCP complex in the lung is to regulate cilial development and orientation in the proximal airways.[23,56]

Several studies have investigated how AEC differentiation and the resulting cell-shape changes, particularly the flattening of AEC1s, contribute to sacculation.[9,57,58] The requirement for both fetal breathing movements[4–8] and the resulting increase in mechanical strain on the epithelium[9,59] have been well established. However, this epithelial-centric focus on sacculation ignores the physical barrier imposed by a thick mesenchymal layer and has left open the question as to whether the mesenchyme might play a more active role in facilitating this stage of morphogenesis. Our study unexpectedly finds that *Vangl1/2* expressed specifically in mesenchymal cells plays a role outside of the core PCP complex to drive the formation of saccules. Saccule-associated mesenchymal cells exhibit elongated and protrusive cell shapes that are correlated with increased cellular motility and tissue fluidity, but loss of Vangl completely disrupts this morphology. Because Vangl is best known for regulating cytoskeletal organization rather than transcriptional output, we postulate that Vangl1/2 regulates cellular motility to increase mesenchymal fluidity, facilitating active thinning of the mesenchymal cell layer. Our data suggest that in the absence of Vangl signaling, the forces from lumenal pressure alone are insufficient to compress mesenchymal cells into the thin layer observed in wild-type lungs at *E*18.5. Rather, we predict that Vangl is part of a complex regulating mesenchymal motility and that a fluid population of mesenchymal cells is essential for normal sacculation.

Early in vertebrate development, the core PCP complex facilitates convergent extension during gastrulation and neural tube closure.[16–18,45] Specifically, PCP complex proteins are required in mesodermal and neuroectodermal tissues,[46,47,60,61] which are planar sheets of cells with some mesenchymal properties at these early stages. During organogenesis, the PCP complex has been primarily described in sheets of epithelial cells but is also known to function in planar mesenchymal tissues, such as the chondrocytes of the developing limb.[41] In these planar tissues, PCP protein complexes are asymmetrically aligned along a single axis (Figure 1A). In contrast, here we show a role for a single PCP component, Vangl1/2, in a complex, nonplanar, three-dimensional (3D) mesenchymal tissue that is shaped similarly to a highly perforated block of Swiss cheese. In such a tissue, there is no single plane of cells. In retrospect, it is logical that core PCP complex function would be dispensable in the pulmonary mesenchyme, as forming a single planar axis of asymmetrically localized protein complexes is physically impossible.

Our study generates exciting new questions that will be investigated in future work. For example, is the fluidity of the mesenchyme a result of directional or random motility? In our mathematical model, mesenchymal cells move randomly under high-pressure, high-fluidity conditions, which is sufficient for saccule expansion. Our *in vivo* work suggests that mesenchymal fluidity is regulated by *Vangl* downstream of *Wnt5a*, and future work will identify how Wnt5a may regulate Vangl function in the lung. Excitingly, a recent study investigating the role of *Wnt5a* in tracheal smooth muscle (TSM) demonstrated that, whereas wild-type TSM cells wrap circumferentially around tracheal epithelium, *Wnt5a*-null TSM cells fail to migrate toward the epithelium, despite maintaining the ability to randomly migrate in an *ex vivo* culture system.[44] That work suggests that *Wnt5a* may be specifically required for directional motion in TSM cells. Perhaps a similar mechanism is at play here, and Vangl regulates not just mesenchymal fluidity but directed motility as well. If so, an important next step will be to understand whether Vangl is asymmetrically localized or asymmetrically activated in pulmonary mesenchymal cells.

Limitations of the study

We believe that a major strength of this study is that all biological experiments were performed in developing lungs, aiding our understanding of how the PCP complex and Vangl1/2 regulate sacculation *in vivo*. However, the physiological complexity of the late-stage embryonic lung and the genetics of the system limited our experimental approaches: we were unable to complete the genetic crosses necessary to determine directly via lineage tracing how depletion of Vangl1/2 affects mesenchymal motility, so we had to rely on a morphological proxy. Finally, although the sacculation phenotype from the mesenchymal *Wnt5a* knockout experiments phenocopy the defects observed in mesenchymal *Vangl1/2* knockout lungs, direct biochemical evidence is required to definitively place Wnt5a upstream of Vangl in a signaling cascade.

STAR★METHODS

Detailed methods are provided in the online version of this paper and include the following:

SUPPLEMENTAL INFORMATION

Supplemental information can be found online at https://doi.org/10.1016/j.devcel.2024.03.010.

ACKNOWLEDGMENTS

We thank Dr. Wei Shi (Keck School of Medicine of USC) for generously providing us with the *Tbx4-rtTA*; *Tet-O-Cre* mice. We are also grateful to Dr. Sha Wang (Microscopy Core Facility at Princeton University) and the University Imaging Center at the University of Minnesota for their assistance with imaging. S.V.P. is very grateful to Katie Little for her work maintaining mice, genotyping, and assisting with revisions. S.V.P. is deeply appreciative of Dr. Maureen Cetera, who hosted S.V.P. in the Cetera Lab at the University of Minnesota to conduct manuscript revisions. This work was supported in part by grants from the National Institutes of Health (HL110335, HL118532, HL120142, HL164861, HD099030, HD111539, AR066070, and AR068320), the Genetics and Molecular Biology Training Grant of the Molecular Biology Department at Princeton University (T32 GM007388), the Camille & Henry Dreyfus Foundation, and a Faculty Scholars Award from the Howard Hughes Medical Institute. S.V.P. was supported in part by a Ruth L. Kirschstein (F31) Fellowship. C.T.-Y. was supported in part by a postdoctoral fellowship from the NJCCR. R.S. was supported in part by the NSF Graduate Research Fellowship Program.

AUTHOR CONTRIBUTIONS

S.V.P., C.M.N., and D.D. conceptualized the study, designed the experiments, interpreted the data, and wrote the manuscript. S.V.P. performed the experiments and collected the data. C.T.-Y. created the mathematical model. R.S. created data-analysis code. All authors provided input on the final manuscript.

DECLARATION OF INTERESTS

The authors declare no competing interests.

Received: January 6, 2023
Revised: October 18, 2023
Accepted: March 8, 2024
Published: April 2, 2024

REFERENCES

1. Metzger, R.J., Klein, O.D., Martin, G.R., and Krasnow, M.A. (2008). The branching programme of mouse lung development. Nature *453*, 745–750. https://doi.org/10.1038/nature07005.

2. Morrisey, E.E., and Hogan, B.L. (2010). Preparing for the first breath: genetic and cellular mechanisms in lung development. Dev. Cell *18*, 8–23. https://doi.org/10.1016/j.devcel.2009.12.010.

3. Desai, T.J., Brownfield, D.G., and Krasnow, M.A. (2014). Alveolar progenitor and stem cells in lung development, renewal and cancer. Nature *507*, 190–194. https://doi.org/10.1038/nature12930.

4. Liggins, G.C., Vilos, G.A., Campos, G.A., Kitterman, J.A., and Lee, C.H. (1981). The effect of spinal cord transection on lung development in fetal sheep. J. Dev. Physiol. *3*, 267–274.

5. Moessinger, A.C., Harding, R., Adamson, T.M., Singh, M., and Kiu, G.T. (1990). Role of lung fluid volume in growth and maturation of the fetal sheep lung. J. Clin. Invest. *86*, 1270–1277. https://doi.org/10.1172/JCI114834.

6. Wigglesworth, J.S., and Desai, R. (1982). Is fetal respiratory function a major determinant of perinatal survival? Lancet *1*, 264–267. https://doi.org/10.1016/s0140-6736(82)90986-2.

7. Perlman, M., Williams, J., and Hirsch, M. (1976). Neonatal pulmonary hypoplasia after prolonged leakage of amniotic fluid. Arch. Dis. Child. *51*, 349–353. https://doi.org/10.1136/adc.51.5.349.

8. Tseng, B.S., Cavin, S.T., Booth, F.W., Olson, E.N., Marin, M.C., McDonnell, T.J., and Butler, I.J. (2000). Pulmonary hypoplasia in the myogenin null mouse embryo. Am. J. Respir. Cell Mol. Biol. *22*, 304–315. https://doi.org/10.1165/ajrcmb.22.3.3708.

9. Li, J., Wang, Z., Chu, Q., Jiang, K., Li, J., and Tang, N. (2018). The Strength of Mechanical Forces Determines the Differentiation of Alveolar Epithelial Cells. Dev. Cell *44*, 297–312.e5. https://doi.org/10.1016/j.devcel.2018.01.008.

10. Nelson, C.M., Gleghorn, J.P., Pang, M.F., Jaslove, J.M., Goodwin, K., Varner, V.D., Miller, E., Radisky, D.C., and Stone, H.A. (2017). Microfluidic chest cavities reveal that transmural pressure controls the rate of lung development. Development *144*, 4328–4335. https://doi.org/10.1242/dev.154823.

11. Unbekandt, M., del Moral, P.M., Sala, F.G., Bellusci, S., Warburton, D., and Fleury, V. (2008). Tracheal occlusion increases the rate of epithelial branching of embryonic mouse lung via the FGF10-FGFR2b-Sprouty2 pathway. Mech. Dev. *125*, 314–324. https://doi.org/10.1016/j.mod.2007.10.013.

12. Poobalasingam, T., Yates, L.L., Walker, S.A., Pereira, M., Gross, N.Y., Ali, A., Kolatsi-Joannou, M., Jarvelin, M.R., Pekkanen, J., Papakrivopoulou, E., et al. (2017). Heterozygous Vangl2(Looptail) mice reveal novel roles for the planar cell polarity pathway in adult lung homeostasis and repair. Dis. Model. Mech. *10*, 409–423. https://doi.org/10.1242/dmm.028175.

13. Yates, L.L., Schnatwinkel, C., Murdoch, J.N., Bogani, D., Formstone, C.J., Townsend, S., Greenfield, A., Niswander, L.A., and Dean, C.H. (2010). The PCP genes Celsr1 and Vangl2 are required for normal lung branching morphogenesis. Hum. Mol. Genet. *19*, 2251–2267. https://doi.org/10.1093/hmg/ddq104.

14. Wang, Y., Guo, N., and Nathans, J. (2006). The role of Frizzled3 and Frizzled6 in neural tube closure and in the planar polarity of inner-ear sensory hair cells. J. Neurosci. *26*, 2147–2156. https://doi.org/10.1523/JNEUROSCI.4698-05.2005.

15. Devenport, D. (2014). The cell biology of planar cell polarity. J. Cell Biol. *207*, 171–179. https://doi.org/10.1083/jcb.201408039.

16. Heisenberg, C.P., Tada, M., Rauch, G.J., Saúde, L., Concha, M.L., Geisler, R., Stemple, D.L., Smith, J.C., and Wilson, S.W. (2000). Silberblick/Wnt11 mediates convergent extension movements during zebrafish gastrulation. Nature *405*, 76–81. https://doi.org/10.1038/35011068.

17. Tada, M., and Smith, J.C. (2000). Xwnt11 is a target of Xenopus Brachyury: regulation of gastrulation movements via Dishevelled, but not through the canonical Wnt pathway. Development *127*, 2227–2238. https://doi.org/10.1242/dev.127.10.2227.

18. Wallingford, J.B., Rowning, B.A., Vogeli, K.M., Rothbächer, U., Fraser, S.E., and Harland, R.M. (2000). Dishevelled controls cell polarity during Xenopus gastrulation. Nature *405*, 81–85. https://doi.org/10.1038/35011077.

19. Curtin, J.A., Quint, E., Tsipouri, V., Arkell, R.M., Cattanach, B., Copp, A.J., Henderson, D.J., Spurr, N., Stanier, P., Fisher, E.M., et al. (2003). Mutation of Celsr1 disrupts planar polarity of inner ear hair cells and causes severe neural tube defects in the mouse. Curr. Biol. *13*, 1129–1133. https://doi.org/10.1016/s0960-9822(03)00374-9.

20. Torban, E., Wang, H.J., Groulx, N., and Gros, P. (2004). Independent mutations in mouse Vangl2 that cause neural tube defects in looptail mice impair interaction with members of the Dishevelled family. J. Biol. Chem. *279*, 52703–52713. https://doi.org/10.1074/jbc.M408675200.

21. Kunimoto, K., Bayly, R.D., Vladar, E.K., Vonderfecht, T., Gallagher, A.R., and Axelrod, J.D. (2017). Disruption of Core Planar Cell Polarity Signaling Regulates Renal Tubule Morphogenesis but Is Not Cystogenic. Curr. Biol. *27*, 3120–3131.e4. https://doi.org/10.1016/j.cub.2017.09.011.

22. Lienkamp, S.S., Liu, K., Karner, C.M., Carroll, T.J., Ronneberger, O., Wallingford, J.B., and Walz, G. (2012). Vertebrate kidney tubules elongate using a planar cell polarity-dependent, rosette-based mechanism of convergent extension. Nat. Genet. *44*, 1382–1387. https://doi.org/10.1038/ng.2452.

23. Vladar, E.K., Bayly, R.D., Sangoram, A.M., Scott, M.P., and Axelrod, J.D. (2012). Microtubules enable the planar cell polarity of airway cilia. Curr. Biol. *22*, 2203–2212. https://doi.org/10.1016/j.cub.2012.09.046.

24. Zhang, K., Yao, E., Lin, C., Chou, Y.T., Wong, J., Li, J., Wolters, P.J., and Chuang, P.T. (2020). A mammalian Wnt5a-Ror2-Vangl2 axis controls the cytoskeleton and confers cellular properties required for alveologenesis. eLife *9*, e53688. https://doi.org/10.7554/eLife.53688.

25. Rao-Bhatia, A., Zhu, M., Yin, W.C., Coquenlorge, S., Zhang, X., Woo, J., Sun, Y., Dean, C.H., Liu, A., Hui, C.C., et al. (2020). Hedgehog-Activated Fat4 and PCP Pathways Mediate Mesenchymal Cell Clustering and Villus Formation in Gut Development. Dev. Cell *52*, 647–658.e6. https://doi.org/10.1016/j.devcel.2020.02.003.

26. Basta, L.P., Hill-Oliva, M., Paramore, S.V., Sharan, R., Goh, A., Biswas, A., Cortez, M., Little, K.A., Posfai, E., and Devenport, D. (2021). New mouse models for high resolution and live imaging of planar cell polarity proteins in vivo. Development *148*, dev199695. https://doi.org/10.1242/dev.199695.

27. Zepp, J.A., Morley, M.P., Loebel, C., Kremp, M.M., Chaudhry, F.N., Basil, M.C., Leach, J.P., Liberti, D.C., Niethamer, T.K., Ying, Y., et al. (2021). Genomic, epigenomic, and biophysical cues controlling the emergence of the lung alveolus. Science *371*, eabc3172. https://doi.org/10.1126/science.abc3172.

28. Yin, H., Copley, C.O., Goodrich, L.V., and Deans, M.R. (2012). Comparison of phenotypes between different vangl2 mutants demonstrates dominant effects of the Looptail mutation during hair cell development. PLoS One *7*, e31988. https://doi.org/10.1371/journal.pone.0031988.

29. Stahley, S.N., Basta, L.P., Sharan, R., and Devenport, D. (2021). Celsr1 adhesive interactions mediate the asymmetric organization of planar polarity complexes. eLife *10*, e62097. https://doi.org/10.7554/eLife.62097.

30. Yin, Y., White, A.C., Huh, S.H., Hilton, M.J., Kanazawa, H., Long, F., and Ornitz, D.M. (2008). An FGF-WNT gene regulatory network controls lung mesenchyme development. Dev. Biol. *319*, 426–436. https://doi.org/10.1016/j.ydbio.2008.04.009.

31. Yu, K., Xu, J., Liu, Z., Sosic, D., Shao, J., Olson, E.N., Towler, D.A., and Ornitz, D.M. (2003). Conditional inactivation of FGF receptor 2 reveals an essential role for FGF signaling in the regulation of osteoblast function and bone growth. Development *130*, 3063–3074. https://doi.org/10.1242/dev.00491.

32. Zhang, W., Menke, D.B., Jiang, M., Chen, H., Warburton, D., Turcatel, G., Lu, C.H., Xu, W., Luo, Y., and Shi, W. (2013). Spatial-temporal targeting of lung-specific mesenchyme by a Tbx4 enhancer. BMC Biol. *11*, 111. https://doi.org/10.1186/1741-7007-11-111.

33. Nishimura, T., Honda, H., and Takeichi, M. (2012). Planar cell polarity links axes of spatial dynamics in neural-tube closure. Cell *149*, 1084–1097. https://doi.org/10.1016/j.cell.2012.04.021.

34. Shi, D., Komatsu, K., Hirao, M., Toyooka, Y., Koyama, H., Tissir, F., Goffinet, A.M., Uemura, T., and Fujimori, T. (2014). Celsr1 is required for the generation of polarity at multiple levels of the mouse oviduct. Development *141*, 4558–4568. https://doi.org/10.1242/dev.115659.

35. Usami, F.M., Arata, M., Shi, D., Oka, S., Higuchi, Y., Tissir, F., Takeichi, M., and Fujimori, T. (2021). Intercellular and intracellular cilia orientation is coordinated by CELSR1 and CAMSAP3 in oviduct multi-ciliated cells. J. Cell Sci. *134*, jcs257006. https://doi.org/10.1242/jcs.257006.

36. Boutin, C., Labedan, P., Dimidschstein, J., Richard, F., Cremer, H., André, P., Yang, Y., Montcouquiol, M., Goffinet, A.M., and Tissir, F. (2014). A dual role for planar cell polarity genes in ciliated cells. Proc. Natl. Acad. Sci. USA *111*, E3129–E3138. https://doi.org/10.1073/pnas.1404988111.

37. Devenport, D., and Fuchs, E. (2008). Planar polarization in embryonic epidermis orchestrates global asymmetric morphogenesis of hair follicles. Nat. Cell Biol. *10*, 1257–1268. https://doi.org/10.1038/ncb1784.

38. Cetera, M., Leybova, L., Woo, F.W., Deans, M., and Devenport, D. (2017). Planar cell polarity-dependent and independent functions in the emergence of tissue-scale hair follicle patterns. Dev. Biol. *428*, 188–203. https://doi.org/10.1016/j.ydbio.2017.06.003.

39. Lu, X., Borchers, A.G., Jolicoeur, C., Rayburn, H., Baker, J.C., and Tessier-Lavigne, M. (2004). PTK7/CCK-4 is a novel regulator of planar cell polarity in vertebrates. Nature *430*, 93–98. https://doi.org/10.1038/nature02677.

40. Andre, P., Wang, Q., Wang, N., Gao, B., Schilit, A., Halford, M.M., Stacker, S.A., Zhang, X., and Yang, Y. (2012). The Wnt coreceptor Ryk regulates Wnt/planar cell polarity by modulating the degradation of the core planar cell polarity component Vangl2. J. Biol. Chem. *287*, 44518–44525. https://doi.org/10.1074/jbc.M112.414441.

41. Gao, B., Song, H., Bishop, K., Elliot, G., Garrett, L., English, M.A., Andre, P., Robinson, J., Sood, R., Minami, Y., et al. (2011). Wnt signaling gradients establish planar cell polarity by inducing Vangl2 phosphorylation through Ror2. Dev. Cell *20*, 163–176. https://doi.org/10.1016/j.devcel.2011.01.001.

42. Wang, S., Roy, J.P., Tomlinson, A.J., Wang, E.B., Tsai, Y.H., Cameron, L., Underwood, J., Spence, J.R., Walton, K.D., Stacker, S.A., et al. (2020). RYK-mediated filopodial pathfinding facilitates midgut elongation. Development *147*, dev195388. https://doi.org/10.1242/dev.195388.

43. Martinez, S., Scerbo, P., Giordano, M., Daulat, A.M., Lhoumeau, A.C., Thomé, V., Kodjabachian, L., and Borg, J.P. (2015). The PTK7 and ROR2 Protein Receptors Interact in the Vertebrate WNT/Planar Cell Polarity (PCP) Pathway. J. Biol. Chem. *290*, 30562–30572. https://doi.org/10.1074/jbc.M115.697615.

44. Kishimoto, K., Tamura, M., Nishita, M., Minami, Y., Yamaoka, A., Abe, T., Shigeta, M., and Morimoto, M. (2018). Synchronized mesenchymal cell polarization and differentiation shape the formation of the murine trachea and esophagus. Nat. Commun. *9*, 2816. https://doi.org/10.1038/s41467-018-05189-2.

45. Goto, T., and Keller, R. (2002). The planar cell polarity gene strabismus regulates convergence and extension and neural fold closure in Xenopus. Dev. Biol. *247*, 165–181. https://doi.org/10.1006/dbio.2002.0673.

46. Nikolopoulou, E., Galea, G.L., Rolo, A., Greene, N.D., and Copp, A.J. (2017). Neural tube closure: cellular, molecular and biomechanical mechanisms. Development *144*, 552–566. https://doi.org/10.1242/dev.145904.

47. Sutherland, A., Keller, R., and Lesko, A. (2020). Convergent extension in mammalian morphogenesis. Semin. Cell Dev. Biol. *100*, 199–211. https://doi.org/10.1016/j.semcdb.2019.11.002.

48. Cetera, M., Leybova, L., Joyce, B., and Devenport, D. (2018). Counter-rotational cell flows drive morphological and cell fate asymmetries in mammalian hair follicles. Nat. Cell Biol. *20*, 541–552. https://doi.org/10.1038/s41556-018-0082-7.

49. Goodwin, K., Jaslove, J.M., Tao, H., Zhu, M., Hopyan, S., and Nelson, C.M. (2022). Patterning the embryonic pulmonary mesenchyme. iScience *25*, 103838. https://doi.org/10.1016/j.isci.2022.103838.

50. Harding, R. (1997). Fetal pulmonary development: the role of respiratory movements. Equine Vet. J. Suppl. *24*, 32–39. https://doi.org/10.1111/j.2042-3306.1997.tb05076.x.

51. Kitterman, J.A. (1996). The effects of mechanical forces on fetal lung growth. Clin. Perinatol. *23*, 727–740. https://doi.org/10.1016/S0095-5108(18)30205-7.

52. Spurlin, J.W., Siedlik, M.J., Nerger, B.A., Pang, M.F., Jayaraman, S., Zhang, R., and Nelson, C.M. (2019). Mesenchymal proteases and tissue fluidity remodel the extracellular matrix during airway epithelial branching in the embryonic avian lung. Development *146*, dev175257. https://doi.org/10.1242/dev.175257.

53. Konopelski Snavely, S.E., Srinivasan, S., Dreyer, C.A., Tan, J., Carraway, K.L., 3rd, and Ho, H.H. (2023). Non-canonical WNT5A-ROR signaling: new perspectives on an ancient developmental pathway. Curr. Top. Dev. Biol. *153*, 195–227. https://doi.org/10.1016/bs.ctdb.2023.01.009.

54. Turcatel, G., Rubin, N., Menke, D.B., Martin, G., Shi, W., and Warburton, D. (2013). Lung mesenchymal expression of Sox9 plays a critical role in tracheal development. BMC Biol. *11*, 117. https://doi.org/10.1186/1741-7007-11-117.

55. Basta, L.P., Sil, P., Jones, R.A., Little, K.A., Hayward-Lara, G., and Devenport, D. (2022). Celsr1 and Celsr2 exhibit distinct adhesive interactions and contributions to planar cell polarity. Front. Cell Dev. Biol. *10*, 1064907. https://doi.org/10.3389/fcell.2022.1064907.

56. Vladar, E.K., Nayak, J.V., Milla, C.E., and Axelrod, J.D. (2016). Airway epithelial homeostasis and planar cell polarity signaling depend on multiciliated cell differentiation. JCI Insight *1*, e88027. https://doi.org/10.1172/jci.insight.88027.

57. Wang, Y., Frank, D.B., Morley, M.P., Zhou, S., Wang, X., Lu, M.M., Lazar, M.A., and Morrisey, E.E. (2016). HDAC3-Dependent Epigenetic Pathway Controls Lung Alveolar Epithelial Cell Remodeling and Spreading via miR-17-92 and TGF-beta Signaling Regulation. Dev. Cell *36*, 303–315. https://doi.org/10.1016/j.devcel.2015.12.031.

58. Frank, D.B., Peng, T., Zepp, J.A., Snitow, M., Vincent, T.L., Penkala, I.J., Cui, Z., Herriges, M.J., Morley, M.P., Zhou, S., et al. (2016). Emergence of a Wave of Wnt Signaling that Regulates Lung Alveologenesis by Controlling Epithelial Self-Renewal and Differentiation. Cell Rep. *17*, 2312–2325. https://doi.org/10.1016/j.celrep.2016.11.001.

59. Huang, Z., Wang, Y., Nayak, P.S., Dammann, C.E., and Sanchez-Esteban, J. (2012). Stretch-induced fetal type II cell differentiation is mediated via ErbB1-ErbB4 interactions. J. Biol. Chem. *287*, 18091–18102. https://doi.org/10.1074/jbc.M111.313163.

60. Butler, M.T., and Wallingford, J.B. (2017). Planar cell polarity in development and disease. Nat. Rev. Mol. Cell Biol. *18*, 375–388. https://doi.org/10.1038/nrm.2017.11.

61. Keller, R., and Sutherland, A. (2020). Convergent extension in the amphibian, Xenopus laevis. Curr. Top. Dev. Biol. *136*, 271–317. https://doi.org/10.1016/bs.ctdb.2019.11.013.

62. Team, R.C. (2021). R: A Language and Environment for Statistical Computing (R Foundation for Statistical Computing).

63. Villanueva, R.A.M., and Chen, Z.J. (2019). ggplot2: Elegant Graphics for Data Analysis. Meas-Interdiscip Res. *17*, 160–167. https://doi.org/10.1080/15366367.2019.1565254.

64. Butler, A., Hoffman, P., Smibert, P., Papalexi, E., and Satija, R. (2018). Integrating single-cell transcriptomic data across different conditions, technologies, and species. Nat. Biotechnol. *36*, 411–420. https://doi.org/10.1038/nbt.4096.

65. Schindelin, J., Arganda-Carreras, I., Frise, E., Kaynig, V., Longair, M., Pietzsch, T., Preibisch, S., Rueden, C., Saalfeld, S., Schmid, B., et al. (2012). Fiji: an open-source platform for biological-image analysis. Nat. Methods *9*, 676–682. https://doi.org/10.1038/nmeth.2019.

66. Berg, S., Kutra, D., Kroeger, T., Straehle, C.N., Kausler, B.X., Haubold, C., Schiegg, M., Ales, J., Beier, T., Rudy, M., et al. (2019). ilastik: interactive machine learning for (bio)image analysis. Nat. Methods *16*, 1226–1232. https://doi.org/10.1038/s41592-019-0582-9.

67. Kibar, Z., Vogan, K.J., Groulx, N., Justice, M.J., Underhill, D.A., and Gros, P. (2001). Ltap, a mammalian homolog of Drosophila Strabismus/Van Gogh, is altered in the mouse neural tube mutant Loop-tail. Nat. Genet. *28*, 251–255. https://doi.org/10.1038/90081.

68. Harfe, B.D., Scherz, P.J., Nissim, S., Tian, H., McMahon, A.P., and Tabin, C.J. (2004). Evidence for an expansion-based temporal Shh gradient in specifying vertebrate digit identities. Cell *118*, 517–528. https://doi.org/10.1016/j.cell.2004.07.024.

69. Harris, K.S., Zhang, Z., McManus, M.T., Harfe, B.D., and Sun, X. (2006). Dicer function is essential for lung epithelium morphogenesis. Proc. Natl. Acad. Sci. USA *103*, 2208–2213. https://doi.org/10.1073/pnas.0510839103.

70. Copley, C.O., Duncan, J.S., Liu, C., Cheng, H., and Deans, M.R. (2013). Postnatal refinement of auditory hair cell planar polarity deficits occurs in the absence of Vangl2. J. Neurosci. *33*, 14001–14016. https://doi.org/10.1523/JNEUROSCI.1307-13.2013.

71. Livet, J., Weissman, T.A., Kang, H., Draft, R.W., Lu, J., Bennis, R.A., Sanes, J.R., and Lichtman, J.W. (2007). Transgenic strategies for combinatorial expression of fluorescent proteins in the nervous system. Nature *450*, 56–62. https://doi.org/10.1038/nature06293.

72. Ryu, Y.K., Collins, S.E., Ho, H.Y., Zhao, H., and Kuruvilla, R. (2013). An autocrine Wnt5a-Ror signaling loop mediates sympathetic target innervation. Dev. Biol. *377*, 79–89. https://doi.org/10.1016/j.ydbio.2013.02.013.

73. Takigawa-Imamura, H., Morita, R., Iwaki, T., Tsuji, T., and Yoshikawa, K. (2015). Tooth germ invagination from cell-cell interaction: Working hypothesis on mechanical instability. J. Theor. Biol. *382*, 284–291. https://doi.org/10.1016/j.jtbi.2015.07.006.

74. Fumoto, K., Takigawa-Imamura, H., Sumiyama, K., Kaneiwa, T., and Kikuchi, A. (2017). Modulation of apical constriction by Wnt signaling is required for lung epithelial shape transition. Development *144*, 151–162. https://doi.org/10.1242/dev.141325.

75. Higaki, T., Takigawa-Imamura, H., Akita, K., Kutsuna, N., Kobayashi, R., Hasezawa, S., and Miura, T. (2017). Exogenous Cellulase Switches Cell Interdigitation to Cell Elongation in an RIC1-dependent Manner in Arabidopsis thaliana Cotyledon Pavement Cells. Plant Cell Physiol. *58*, 106–119. https://doi.org/10.1093/pcp/pcw183.

76. Fumoto, K., Takigawa-Imamura, H., Sumiyama, K., Yoshimura, S.H., Maehara, N., and Kikuchi, A. (2019). Mark1 regulates distal airspace expansion through type I pneumocyte flattening in lung development. J. Cell Sci. *132*, jcs235556. https://doi.org/10.1242/jcs.235556.

77. Aigouy, B., Farhadifar, R., Staple, D.B., Sagner, A., Röper, J.C., Jülicher, F., and Eaton, S. (2010). Cell flow reorients the axis of planar polarity in the wing epithelium of Drosophila. Cell *142*, 773–786. https://doi.org/10.1016/j.cell.2010.07.042.

78. Aw, W.Y., Heck, B.W., Joyce, B., and Devenport, D. (2016). Transient Tissue-Scale Deformation Coordinates Alignment of Planar Cell Polarity Junctions in the Mammalian Skin. Curr. Biol. *26*, 2090–2100. https://doi.org/10.1016/j.cub.2016.06.030.

Please cite this article in press as: Paramore et al., *Vangl*-dependent mesenchymal thinning shapes the distal lung during murine sacculation, Developmental Cell (2024), https://doi.org/10.1016/j.devcel.2024.03.010

STAR★METHODS

KEY RESOURCES TABLE

REAGENT or RESOURCE	SOURCE	IDENTIFIER
Antibodies		
SPC (rabbit)	Millipore, Cat# ab3786	RRID: AB_91588
RAGE (rat)	R&D, Cat# MAB1179	RRID: AB_2289349
Ecad (rat)	Invitrogen, Cat# 14-3249-82	RRID: AB_1210458
Ecad (rabbit)	Cell Signaling, Cat# 3195	RRID: AB_2291471
Celsr1 (guinea pig)	Custom (Danelle Devenport)	N/A
Vangl2 (rat)	Millipore, Cat# MABN750	RRID: AB_2721170
GFP (chicken)	Abcam, Cat# ab13970	RRID: AB_300798
RFP (rabbit) [recognizes tdTom]	Rockland Inc, Cat# 600-401-379	RRID: AB_2209751
αSMA (mouse)	Sigma, Cat# a5228	RRID: AB_262054
CD31 (rabbit)	Abcam, Cat# ab28364	RRID: AB_726362
Sox9 (rabbit)	Millipore	Cat# AB5535; RRID: AB_2239761
Phospho-Histone-3 (rabbit)	Upstate (Millipore), Cat# 06-570	RRID: AB_310177
Cleaved Caspase-3 (rabbit)	Cell Signaling, Cat# 9661S	RRID: AB_2341188
Alexa Fluor® 488 donkey anti-rat	Invitrogen, Cat# A-21208	RRID: AB_141709
Alexa Fluor® 594 donkey anti-rat	Jackson ImmunoResearch, Cat# 712-585-150	RRID: AB_2340688
Alexa Fluor® 647 donkey anti-rat	Jackson ImmunoResearch, Cat# 712-605-153	RRID: AB_2340694
Alexa Fluor® 488 donkey anti-rabbit	Jackson ImmunoResearch, Cat# 711-545-152	RRID: AB_2313584
Alexa Fluor® 555 donkey anti-rabbit	Invitrogen, Cat# A-31572	RRID: AB_162543
Alexa Fluor® 647 donkey anti-rabbit	Invitrogen, Cat# A-31573	RRID: AB_2536183
Alexa Fluor® 488 donkey anti-chick	Jackson ImmunoResearch, Cat# 703-545-155	RRID: AB_2340375
Alexa Fluor® 647 donkey anti-guinea pig	Jackson ImmunoResearch, Cat# 706-605-148	RRID: AB_2340476
Alexa Fluor® 555 donkey anti-mouse	Invitrogen, Cat# A-31570	RRID: AB_2536180
Chemicals, peptides, and recombinant proteins		
Fish gelatin	Sigma, Cat# G7765	N/A
Bovine serum albumin	Sigma, Cat# A7906	N/A
Triton X-100	Sigma, Cat# X100	N/A
Normal donkey serum	Sigma, Cat# D9663	N/A
ProLong™ Gold Antifade Mountant	Thermo Fisher, Cat# P36930	N/A
Doxycycline hyclate	Sigma, Cat# D9891	N/A
Hoechst	Invitrogen, Cat# H1399	N/A
Deposited data		
*E*17 mouse lung single cell RNA sequencing data	(Zepp et al.)[27]	GSE149563
Code for computational model of sacculation	Deposited on Zenodo	https://zenodo.org/records/10779328
Experimental models: Organisms/strains		
Vangl2^{Lp}	The Jackson Laboratory	JAX: 000220
Celsr1^{Crsh}	Elaine Fuchs, Jen Murdoch, originally published in Curtin et al.[19]	MGI: 2668337
Shh$^{tm1(EGFP/cre)Cjt}$	The Jackson Laboratory	JAX: 005622
Twist2$^{tm1.1(cre)Dor}$	The Jackson Laboratory	JAX: 008712
Tbx4-rtTA	Gift from Wei Shi, originally published in Zhang et al.[32]	N/A
tet-O-Cre	The Jackson Laboratory	JAX: 006234
Vangl1 flox (*Vangl1*$^{tm1.1Nat}$)	The Jackson Laboratory	JAX: 019518

(*Continued on next page*)

Please cite this article in press as: Paramore et al., *Vangl*-dependent mesenchymal thinning shapes the distal lung during murine sacculation, Developmental Cell (2024), https://doi.org/10.1016/j.devcel.2024.03.010

Continued

REAGENT or RESOURCE	SOURCE	IDENTIFIER
Vangl2 flox (*Vangl2*$^{tm2.1Mdea}$)	The Jackson Laboratory	JAX: 025174
Wnt5a flox (*Wnt5a*$^{tm1.1Krvl}$)	The Jackson Laboratory	JAX: 026626
mTmG reporter: (*Gt(ROSA)26Sor*$^{tm4(ACTB-tdTomato,-EGFP)Luo}$)	The Jackson Laboratory	JAX: 007676
Confetti reporter: (*Gt(ROSA)26Sor*$^{tm1(CAG-Brainbow2.1)Cle}$)	The Jackson Laboratory	JAX: 017492
Oligonucleotides (Genotyping Primers)		
Allele being genotyped	Forward Primer	Reverse Primer
Cre (used for all lines)	GCATTACCGGTCGATGCAACGAGTGATGAG	GAGTGAACGAACCTGGTCGAAATCAGTGCG
Vangl1 flox	ACATGATCACACCAATTCTGTCCA	CTGGACTCACACTCTACCTCAATGGCA
Vangl2 flox	TCCTGTCCCTGAGTCCCAAATG	CTACTCCAGCCTGCGCCAACCTTA
Celsr1^{Crsh} (PCR)	TGCTACAGACCGTGACTCAG	TGCCCTCCACGATCTGATAC
Celsr1^{Crsh} (sequencing)	GGTGGGGATGATGGAGATGG	
Vangl2 WT allele	CAAACAGTGGACCTTGGTGTG	TGGCAGAAATGTGTCAGGG
Vangl2^{Lp}	CAAACAGTGGACCTTGGTGTA	TGGCAGAAATGTGTCAGGG
Tbx4-rtTA	GGAAGGCGAGTCATGGCAAGA	AGGTCAAAGTCGTCAAGGGCAT
Wnt5a flox	GGTGAGGGACTGGAAGTTGC	GGAGCAGATGTTTATTGCCTTC
GFP (for Confetti genotyping)	ACGGCCACAAGTTCAGC	CGTCGCCGATGGGGGTGTTCT
Software and algorithms		
Imaris	Oxford Instruments	https://imaris.oxinst.com/
MATLAB	Mathworks	https://www.mathworks.com/?s_tid=gn_logo
R Studio	Program and code from Team[62] and Villaneueva and Chen[63]	https://posit.co/download/rstudio-desktop/
Seurat	Originally published in Butler et al.[64]	https://satijalab.org/seurat/
FIJI	Program and code from Schindelin et al.[65]	https://imagej.net/software/fiji/
Ilastik	Program and code from Berg et al.[66]	https://www.ilastik.org

RESOURCE AVAILABILITY

Lead contact

Further information and requests for resources and reagents should be directed to and will be fulfilled by the lead contact, Danelle Devenport (danelle@princeton.edu).

Materials availability

This study did not generate new unique reagents.

Data and code availability

- Single-cell RNA-sequencing data analyzed in this manuscript are deposited at GEO and are publicly available. Accession numbers are listed in the key resources table. Microscopy data reported in this paper will be shared by the lead contact upon request.
- All original code has been deposited at Zenodo and is publicly available as of the date of publication. Links for access are listed in the key resources table.
- Any additional information required to reanalyze the data reported in this paper is available from the lead contact upon request.

EXPERIMENTAL MODEL AND STUDY PARTICIPANT DETAILS

Mouse lines and breeding

All procedures involving animals were approved by Princeton University's Institutional Animal Care and Use Committee (IACUC). Mice were bred and maintained under standard laboratory conditions receiving food and water *ad libitum* in an AAALAC-accredited facility in accordance with the NIH Guide for the Care and Use of Laboratory Animals. This study was compliant with all relevant ethical regulations regarding animal research. Embryos of both sexes were used for all experiments. All strains were maintained

Please cite this article in press as: Paramore et al., *Vangl*-dependent mesenchymal thinning shapes the distal lung during murine sacculation, Developmental Cell (2024), https://doi.org/10.1016/j.devcel.2024.03.010

on a Bl6 background unless otherwise stated. *Celsr1-3xGFP*, *Fzd6-3xGFP,* and *tdTomato-Vangl2* mouse lines were used to assess the localization of core PCP proteins during lung development.[26] *Vangl2*$^{Lp/Lp}$ embryos[67] and *Celsr1*$^{Crsh/Crsh}$ embryos[19] were used to determine how loss of PCP function affects sacculation. The *Celsr1*$^{Crsh/Crsh}$ strain was maintained on a mixed (Bl6 and C3H) background. *ShhCreGFP; Vangl1*$^{fl/fl}$*; Vangl2* $^{fl/fl}$*; Rosa26mTmG/Rosa26mTmG* embryos were used to conditionally delete *Vangl1/2* from the lung epithelium.[68–70] *Dermo1Cre; Vangl1* $^{fl/fl}$*; Vangl2* $^{fl/fl}$*; Rosa26mTmG/Rosa26mTmG* embryos were used to conditionally delete *Vangl1/2* from the pulmonary mesenchyme.[30,31] *Tbx4-rtTA; Tet-O-Cre; Vangl1* $^{fl/fl}$*; Vangl2* $^{fl/fl}$*; Rosa26mTmG/Rosa26mTmG* embryos were used to conditionally delete *Vangl1/2* from the pulmonary mesenchyme in an inducible manner.[32] To induce full *Vangl1/2* deletion, both doxycycline-medicated water (0.5 mg/mL) and an intraperitoneal injection (0.1 mg doxycycline/1 g weight) were administered to pregnant dams at *E*14. *Tbx4-rtTA; Tet-O-Cre; R26R-Confetti*[71] embryos were used for lineage-labeling and cell-shape analysis. *Tbx4-rtTA; Tet-O-Cre; Vangl1* $^{fl/fl}$*; Vangl2* $^{fl/fl}$*; R26R-Confetti* embryos were used for cell-shape analysis. *ShhCreGFP; Wnt5a* $^{fl/fl}$ embryos were used to conditionally delete *Wnt5a* from the lung epithelium.[72] *Tbx4-rtTA; TetO-Cre; Wnt5a* $^{fl/fl}$ embryos were used to conditionally delete *Wnt5a* from the pulmonary mesenchyme in an inducible manner; doxycycline was administered in water at *E*15 as described above. Mouse strains and relevant genotyping primers are detailed in the key resources table.

METHOD DETAILS

Immunofluorescence analysis

Lungs and tracheas were dissected from embryos in PBS and fixed in 4% paraformaldehyde (PFA). All tracheas were fixed for 1 h at 4°C, washed with PBS, incubated overnight in blocking buffer composed of 4% normal donkey serum, 1% bovine serum albumin (BSA), and 1% fish gelatin in PBT2 (PBS with 0.2% Triton X-100), washed with PBS, incubated with primary antibody overnight, washed with PBS, and incubated with secondary antibody overnight. Tracheas were then washed and mounted on a slide for imaging in Prolong Gold. *E*13.5 lungs were fixed for 30 min at 4°C. *E*16-18.5 lungs were fixed for 1 h at 4°C. Lungs were washed in PBS and taken through a sucrose gradient before embedding in OCT. 10-μm-thick and 200-μm-thick frozen sections were obtained from samples using a Leica CM3050S cryostat. 10-μm-thick sections were washed in PBT3 (PBS with 0.3% Triton X-100), washed in PBS, incubated in blocking buffer for 1 h at room temperature, and then incubated in blocking buffer with primary antibody overnight. Slides were then washed in PBS and incubated with secondary antibody for 3 h and mounted in Prolong Gold. 200-μm-thick floating sections were washed in PBT3, washed in PBS, incubated in blocking buffer overnight at 4°C, and then incubated in blocking buffer with primary antibody overnight. Sections were then washed in PBS and incubated with secondary antibody overnight at 4°C. Sections were then washed in PBS and mounted in Prolong Gold. Antibodies used for staining are detailed in the key resources table.

Computational model of sacculation

To test the role of mesenchymal fluidity during sacculation, we created a 2D agent-based model of particles (cells) undergoing Brownian motion, as described by their center of mass. The model combines epithelial and mesenchymal compartments in which cells are reduced to their center points and packed such that they do not overlap. The motion of a cell in each compartment is affected by its interactions with neighboring cells and fluctuations in the system. The equations of motion for the positions of cells in both compartments are considered in the overdamped limit, which is commonly used to describe biological systems where the inertial effects are much smaller than the effects from intracellular interactions or the fluctuations in the system.

We modeled the mesenchyme as a collection of cells, where each cell is reduced to its center and is driven by a Langevin-like equation in continuous time. The equation of motion for a mesenchymal cell *i* is described as follows:

$$\frac{d\overline{x}_i}{dt} = \mu_m \overline{F}_i^m \qquad \text{(Equation 1)}$$

where $\overline{x}_i$ is the position of cell *i*, μ_m is the motility coefficient for the mesenchymal population, and $\overline{F}_i^m$ is the sum of all forces acting upon the *i*th mesenchymal cell

$$\overline{F}_i^m = f_a \overline{n}_i + \sum\nolimits_{i \neq j} \overline{F}_{ij}^{interaction} \qquad \text{(Equation 2)}$$

The term $f_a \overline{n}_i$ models the internal cellular processes that drive a mesenchymal cell to move in the direction of its polarity, and the interaction between the *i*th cell and its nearest neighbors[9,73–76] is defined as:

$$\overline{F}_{ij}^{interaction} = kf\left(\frac{\overline{d}_{ij}}{d_0}\right)\frac{(\overline{x}_i - \overline{x}_j)}{|\overline{x}_i - \overline{x}_j|} \qquad \text{(Equation 3)}$$

$$f(\xi) = \begin{cases} \xi^{\lambda} + \left(\frac{\xi_{\text{cutoff}}}{\xi}\right)^{\lambda} - 1 - (\xi_{\text{cutoff}})^{\lambda} \text{ for } 0 < \xi \leq \xi_{\text{cutoff}} \\ 0 \text{ for } \xi > \xi_{\text{cutoff}} \end{cases}$$

Please cite this article in press as: Paramore et al., *Vangl*-dependent mesenchymal thinning shapes the distal lung during murine sacculation, Developmental Cell (2024), https://doi.org/10.1016/j.devcel.2024.03.010

where $\overline{F}_{ij}$ is the force between *i*th and *j*th mesenchymal cells (repulsive at short distances and attractive at longer distances), *k* describes the strength of the interaction force, and $\overline{d}_{ij}$ *is* the distance between the cells calculated as $\overline{d}_{ij} = \left|\overline{x}_i - \overline{x}_j\right|$. The optimal value $d_0 = r_i + r_j$ is the optimal distance between two cells. To simplify the model, we fixed the optimal distance to $d_0 = 1$ (Figure 5A). Cell-cell interactions are also assumed to occur indirectly between the mesenchyme and the epithelium using the same force defined in Equation 3, so that the deformation of the epithelial tissue is coupled to that of the surrounding mesenchyme. The parameters are ξ_{cutoff} =1.63, $\lambda = 2,$ and k =1.

The polarity vector $\overline{n}_i = (\cos\vartheta_i, \sin\vartheta_i)$ is modeled as a Gaussian white rotational noise:

$$\frac{d\vartheta_i}{dt} = \xi_i(t) \quad \text{(Equation 4)}$$

where $\xi_i(t)$ is a white noise with zero mean $\langle\xi_i(t)\rangle = 0$ and correlations $\langle\xi_i(t)\xi_j(t')\rangle = 2D_r\delta_{ij}\delta(t - t')$. D_r measures the average magnitude of the stochastic force and is a rotational diffusion coefficient.

We modeled the structure of the epithelium as a 2D chain of cells distributed in a single layer that initially conformed to the circumference of a saccule. The equation of motion for an epithelial cell *i* is described as:

$$\frac{d\overline{x}_i}{dt} = \mu_e\overline{F}_i^e \quad \text{(Equation 5)}$$

where μ_e is the motility coefficient for the epithelium, and $\overline{F}_i^e$ denote the summations of the forces acting upon the *i*th epithelial cell

$$\overline{F}_i^e = \overline{F}_i^{bending} + \sum_{i\neq j}\overline{F}_{ij}^{interaction} + \overline{F}_i^{pressure} \quad \text{(Equation 6)}$$

The forces are considered to mimic the deformation of the epithelium observed experimentally. The effect of bending is incorporated to align the cells and obtain a smooth outline of the epithelium[9,73–76] as follows

$$\overline{F}_i^{bending} = k^{bend}\left(\frac{\theta_i - \theta_{i-1}}{\left|\overline{x}_i - \overline{x}_{i-1}\right|}\overline{n}_{i-1} + \frac{\theta_i - \theta_{i+1}}{\left|\overline{x}_i - \overline{x}_{i+1}\right|}\overline{n}_i\right) \quad \text{(Equation 7)}$$

where θ_i represents the angle between the vectors $\overline{x}_i - \overline{x}_{i-1}, \overline{x}_{i+1} - \overline{x}_i, \overline{n}_i$ is a unit vector normal to $\overline{x}_{i+1} - \overline{x}_i\left(\frac{\pi}{2} - rotation\right)$, and k^{bend} is the bending elasticity coefficient. Interactions between epithelial cells were modeled using Equation 3.

Expansion of the epithelium in response to lumenal fluid pressure[9,73–76] was modeled by incorporating an outward force on the epithelial cells as

$$\overline{F}_i^{pressure} = -k^{press}(\overline{n}_{i-1} + \overline{n}_i) \quad \text{(Equation 8)}$$

where k^{press}represents its magnitude.

Although the output of the simulations represents the epithelium as a continuous line, the simulated tissue is comprised of discrete cells whose interactions are within a distance ξ_{cutoff} =1.63 (see pink curve Figure 5A). *In vivo*, epithelial surface area increases because of cell-shape changes; to simplify the model, the increase in epithelial surface area *in silico* is accounted for by increased epithelial cell division instead. Cell proliferation was implemented computationally by measuring the distance between two adjacent cells. If the distance is larger than d = 0.5, one cell is added in between two pre-existing epithelial cells. This approach allowed us to model the growth and deformation of the epithelium.

QUANTIFICATION AND STATISTICAL ANALYSIS

Quantification of Celsr1 polarity

Celsr1 polarity was calculated using Packing Analyzer V2 software[77] as previously described.[78] The software measures the axis and magnitude (nematic order) of junctional polarity. Cells were segmented using the E-cadherin signal. The angles were plotted in a circular histogram using the polar plot function in MATLAB. The magnitude of polarity and orientation of average Celsr1 polarity were overlaid as a line on top of the histogram, where the length of the line and its orientation reflect the magnitude and direction of Celsr1 polarity.

Single-cell RNA-sequencing (scRNA-seq) analysis

We analyzed a previously published scRNA-seq dataset (GSE149563)[27] generated from *E*17.5 mouse lungs. This analysis was carried out using the Seurat package.[64] The data were first filtered to exclude cells with fewer than 500 genes, more than 30,000 unique molecular identifiers (possible multiplets), and greater than 10% mitochondrial DNA (dying cells). Following the Seurat pipeline, we then normalized the data, identified variable features, scaled gene expression for each cell, ran principal components analysis, and identified neighbors and clusters. We then generated uniform manifold approximation and projection (UMAP) plots and extracted cluster markers to identify cell types. Clusters from the *E*17.5 lung dataset representing distinct cell types were annotated based on the most highly expressed genes in each cluster. We then examined the expression patterns of genes of interest by color-coding the UMAP and comparing cell-level expression of these genes in different cell clusters.

Please cite this article in press as: Paramore et al., *Vangl*-dependent mesenchymal thinning shapes the distal lung during murine sacculation, Developmental Cell (2024), https://doi.org/10.1016/j.devcel.2024.03.010

Sacculation analysis

Tiled 20× images of entire lung sections were acquired on a Nikon A1RSi confocal microscope. Sections were imaged for RAGE, SPC, and Hoechst, or for mTmG, RAGE, and Hoechst when applicable. To calculate the area of tissue, the image was first binarized using FIJI[65] such that non-tissue regions were labeled in white. After binarization, this image was negated and the sum of the white (tissue) pixels was calculated, giving the value of the area of the tissue.

To calculate the area and perimeter of each saccule from a given image, the image was first binarized where the saccules were labeled in white. The area and perimeter were then calculated for each saccule using the 'regionprops' function in MATLAB. This value was then converted to units of μm^2. Any saccule smaller than 50 μm^2 (for images with no transgenic mTmG) or 25 μm^2 (for images with transgenic mTmG) was filtered out and discarded from further analysis.

Quantification of Vangl2 intensity

60× images of lung sections were acquired on a Nikon A1RSi or Nikon AXR confocal microscope. Sections were imaged for Vangl2 and Ecad or for Vangl2, phalloidin, and Sox9. Ecad signal or phalloidin and Sox9 signal were used to identify and mask Vangl2 signal from the epithelial compartment. Using FIJI, the corrected total mesenchymal Vangl2 fluorescence was calculated as follows:

$$\textit{integrated density of mesenchymal region} - (\textit{area of mesenchymal region} * \textit{mean gray value of background region})$$

Lumenal areas were used to identify the mean gray value of background region, as they lack Vangl2 protein. Three images were quantified per lung; each lung's corrected total mesenchymal Vangl2 fluorescence represents the average of all images per lung.

Lineage-tracing analysis

For each cell of each clone (simulated and *in vivo*), the center point was determined by identifying the xy coordinates using FIJI. The center point was then graphed using a custom MATLAB script where, for each clone, the clone centroid was calculated by the mean of each point. The distance from the center of each cell to its clone centroid was calculated as the Euclidean distance. Plots were then generated where each center point of each cell of a clone was subtracted by the centroid of that clone. These clone-centroid subtracted points were then overlayed on top of each other and color coded by embryonic stage.

Mesenchymal cell-shape analysis

Images of RFP-labeled saccule-associated mesenchymal cells were obtained only from the saccular regions of the lung; mesenchyme adjacent to conducting airways was not imaged to avoid including airway smooth muscle cells in this analysis. Saccule-adjacent mesenchymal cells were segmented and binarized using the ilastik 2-stage autocontext workflow,[66] using the signal from cytoplasmic RFP^+ mesenchymal cells. Segmented images were then analyzed in MATLAB by labeling each connected component using the bwlabel function. The segmented cell metrics of perimeter, area, convex hull area, circularity, and major and minor axis lengths were then calculated using the regionprops function. Area/convex hull area was calculated as the ratio between area and convex hull area. Aspect ratio was calculated as the ratio of the major and minor axis lengths. Shape factor was calculated as the ratio of the perimeter and the square root of the area. Histograms were then generated using R and the ggplot2 package.[62,63]